© Copyright 2021

Arman Reza Naderi

Rapidly prototyping complex microfluidics through stereolithography

Arman Reza Naderi

A thesis

submitted in partial fulfillment of the

requirements for the degree of

Master of Science in Bioengineering

University of Washington

2021

Supervisory Committee:

Albert Folch

Alshakim Nelson

Program Authorized to Offer Degree:

Bioengineering

University of Washington

Abstract

Rapidly prototyping complex microfluidics through stereolithography

Arman Reza Naderi

Chair of the Supervisory Committee:

Albert Folch

Department of Bioengineering

Keywords: microfluidics, stereolithography, polymer chemistry, organ-on-a-chip, finite element analysis

As organ-on-a-chip research becomes more popular, greater effort is being placed into creating *in vitro* cell culture systems that more accurately represent the complexity of *in vivo* biology. Microfluidics, or the manipulation and analysis of microliter-scale fluids in micro-channels and chambers, have enabled the creation of increasingly complex 3D cell culture platforms that can better represent organ-level functionality. For decades, micromolded polydimethylsiloxane (PDMS) has been the predominant microfluidics prototyping tool because of its high-resolution patterning, biocompatibility, and optical transparency. However, the disadvantages associated with its manufacturability, and thus its rapid prototypability, limits the prospect of using PDMS for future organ-on-a-chip systems. This work aims to demonstrate the advantages of digital manufacturing

and stereolithography for the production, testing, and development of complex microfluidic devices. Through the addition of novel monomers to stereolithography resin formulations, I proved that the functionalization of 3D printable hard plastic was possible with essentially any biomolecule of interest. These materials can then be used to produce high resolution structures in all three spatial dimensions, enabling the fabrication of unique structures that can only be fabricated through stereolithography. A hard plastic muscle cell-in-gel culture system was developed for long-term culture, differentiation, and fusion of myocytes into myotubes. Then, a finite element analysis program was used to prototype a microfluidic device capable of producing complex, 3D gradients within short timescales; the device was tested using colorimetric reagents. Lastly, a microfluidic microneedle array was tested to help improve the efficacy of induced pluripotent stem cell delivery during intramyocardial injection of infarcted heart tissues. By proving stereolithography is a valuable tool for microfluidic device fabrication, testing, and rapid prototyping, I aim to increase its implementation and dissemination as a means of experimenting with more biologically representative *in vitro* models.

Acknowledgements

I would first like to sincerely thank my advisor, Dr. Albert Folch, for taking a chance 5 years ago to provide me with my first ever research opportunity as a freshman at the University of Washington. Ever since that moment, Dr. Folch has allowed me to take intellectual ownership of my work, guided me through so many difficult challenges associated with research, and pushed me to become a better scientist, engineer, and educator. His expertise and vision for new research continue to be an inspiration for me. I would also like to thank my co-advisor, Dr. Alshakim Nelson, for his continued generosity in supporting my research efforts. Whether it be spending time to expertly explain the intricacies of polymer chemistry or offering the assistance of his talented students to troubleshoot an experiment, Dr. Nelson is a glowing example of the ideal research collaborator.

This work would not have been possible without the assistance of Dr. Lisa Horowitz. Dr. Horowitz is a tireless colleague who was always willing to provide invaluable insight into improving my scientific methodology. I am grateful to have learned from such a phenomenal scientist. I would also like to thank Allison Zech (working under Dr. Stephen Seslar) and Claudia Willis, Dr. Dylan Karis, and Dr. Christopher Fellin (all working under Dr. Alshakim Nelson) for their collaboration on the many different projects covered within this work. Without their assistance, much of the presented progress would not have been possible. Similarly, I want to show my appreciation to the other members of the Folch lab for their support and collaboration. I am very grateful to have worked and learned alongside so many talented young scientists and engineers.

I would also like to acknowledge the financial support I received through Dr. Albert Folch and the University of Washington's Work Study program. It enabled me to conduct this work amid an unprecedented pandemic.

Lastly, I must express my sincere admiration and gratitude to my parents, sisters, and friends for providing undying support and constant encouragement throughout my years of study and research. I would not be here without each one of you. You inspire me every day. Thank you.

Table of contents

List of figures

List of tables

1. Introduction

Drug discovery, cancer research, and regenerative medicine depend on *in vitro* cell culture to study the formation, physiology, and function of cells. *In vitro* cultures enable researchers to control and study a simplified cellular microenvironment meant to replicate the essential physiology of tissues found *in vivo*. Two-dimensional (2D) cell monolayers are the conventional culture paradigm used in the lab and clinic because of low material and maintenance costs and high scalability. Quantitative and qualitative measurement techniques have developed around *in vitro* cell culture to aid in cell biology analysis. For example, fluorescent staining techniques enable the observation of cell formation and physiology via microscopy, and gene expression markers can be measured via automated and manual methods to assess cell function. These analysis techniques reveal that 2D cell monolayers fail to represent the complex biology of cells found *in vivo* [1], [2]. Limited to chemically homogeneous, planar systems, 2D cell culture platforms have significant phenotypic differences in development, morphology, and protein expression compared to cells in their native, three-dimensional (3D) tissues. 3D cell culture platforms overcome these limitations by preserving or recreating the spatial complexity of human cell-cell, cell-nutrient source, and cell-extracellular matrix (ECM) interactions in an *ex vivo* microenvironment. Cell culture platforms that incorporate 3D cellular interactions cause cells to have distinct transcriptional profiles that more closely resemble native tissue compared to their 2D counterparts [3], [4]. These transcriptomic differences result in observable changes in morphology and development for stem, tumor, and primary cells cultured in 2D versus 3D microenvironments. Microfluidics, or the manipulation and analysis of microliter-scale fluids in micro-channels and chambers, have enabled the creation of increasingly complex 3D cell culture platforms that can better represent organ-level functionality.

Organ-on-a-chips, also known as microphysiological systems, are microscale, *in vitro* models of human physiology that reconstitute a variety of organ-level functions for drug screening, diagnostic, and therapeutic applications. These microfluidic devices can mimic *in vivo* responses by

using human cell lines retrieved via organ donors or human induced pluripotent stem cells (hiPSCs). Organ-on-a-chips have already been demonstrated as effective organ models for the liver, kidney, and lungs [5]. Advances in microfabrication technology, such as micromolding and soft lithography, have allowed for the creation of sophisticated, 3D microenvironments that facilitate tissue-tissue interfaces, spatiotemporal chemical gradients, and dynamic fluidic and mechanical interactions [6], [7]. The vast majority of organ-on-a-chips are fabricated using micromolded polydimethylsiloxane (PDMS), wherein 3D structures are created by manually stacking, precisely aligning, and then bonding microfluidic layers [8]. PDMS is a popular prototyping tool for microfluidics because it is a transparent, cytocompatible material that has a high resolution (<1 μm features possible) molding procedure. Although organ-on-a-chips are powerful tools that enable unique biological studies, their implementation into broader healthcare research markets is limited by PDMS micromolding for two key reasons. First, PDMS strongly absorbs small hydrophobic molecules such as drugs or hormones, which can confound the results of biological studies or pre-clinical/clinical trials due to cross-contamination issues [9], [10]. Second, the creation of complex, 3D PDMS microfluidic devices requires multilayer assembly and bonding which restricts high-throughput manufacturability. Furthermore, the preparation of a master mold can take days to weeks, limiting the rapid prototyping of PDMS devices. In the past decade, advances in digital manufacturing techniques have made microfluidic device creation more widely available by addressing the material and fabrication constraints of PDMS micromolding.

Digital manufacturing is an integrated production method in which computers are used for modular 3D design, performance simulation, automated fabrication, assembly, and quality control [11]. All digital manufacturing methods share (*a*) the ability to produce a physical device from a digital design file and (*b*) the ability to encode the fabrication process as a set of parameters; importantly, both the design file and the process parameters can be electronically sent to distant collaborators operating a similar machine in order to produce a replica of the local print. One of the

most widely used digital manufacturing methods is 3D printing, an additive manufacturing technique that can be used to create hard plastic or hydrogel constructs for bioengineering applications.

Stereolithography (SL) is a form of 3D printing that allows for the assembly-free simultaneous production of quasi-arbitrary 3D shapes in a single polymeric material from a liquid photoresin precursor by means of a UV light source, such as a digital light projector (DLP). A 3D object is built using selective light exposure to photopolymerize the precursor resin collected in a vat. In the layer-by-layer approach, each layer is projected as an image obtained by digitally sectioning the 3D object into thin slices [12]. For microfluidics, where a transparent resin is desirable, a UV light source becomes necessary since transparent resins feature low absorption (and thus poor resolution in the visible range) [13]. In modern desktop systems, the resin is squeezed into thin layers by a motorized build plate and exposed to light by a UV-LED array. In DLP-based SL, the XY resolution is limited by the size of the projected pixels, and the Z resolution is determined by the resolution of the Z motor and the resin composition. A schematic for the bat configuration of a DLP SL printer is shown in Figure 1. The minimum cross-sectional area of a microchannel that is attainable by SL depends not only on the pixel resolution but also on the type and viscosity of the resin, which has to be effectively drained from the channels post-printing [14]. The minimum feature size that is achievable by SL is dependent on the pixel size, the absorption spectra of the photoresin, and the diffusivity of the reactants [15]. In SL, a microchannel is built by photopolymerizing the channel walls and roof then draining the uncured resin from the channel cavity after the printing is complete [16], [17]. This process limits the choice of SL resins since the final print must be at the very least transparent and, for organ-on-a-chip applications, biocompatible as well.

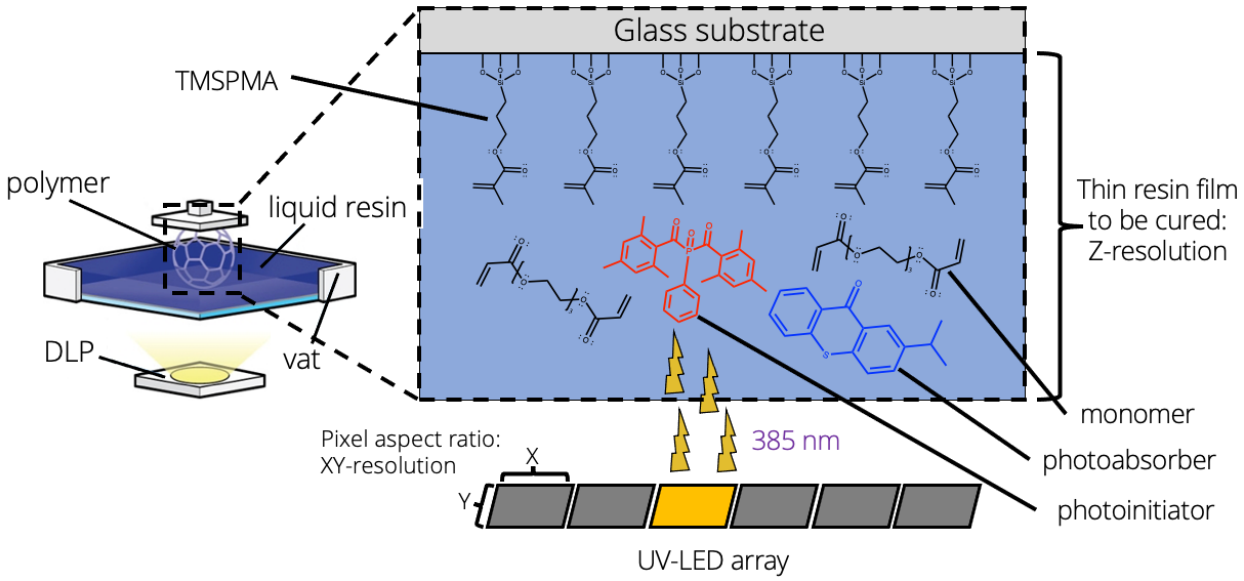

Figure 1: Schematic of the bat configuration of a DLP-SL printer. Light emitted from a UV-LED array shines through a transparent-bottom vat that contains a photo-sensitive, liquid resin. The light is absorbed by photoinitiators (OM819) dissolved in the resin which generate reactive species, such as radicals, when exposed to radiation. These radicals attack acrylate-based monomers (PEGDA-258) in the resin, initiating radical polymerization. The monomer propagates the radical chain reaction, growing the polymer in length by binding to acrylate-substrates on a build plate. After UV-LED light exposure stops, the radical polymerization reaction proceeds to terminate. In the bat configuration, the first layer of polymer is bonded to a glass substrate via an acrylate-functionalizing linker (TMSPMA, see Appendix 8.1); all subsequent layers of polymer are built off this first polymer layer. The z-resolution of the printer determines microchannel formation capability. The motorized build plate pushes resin into thin layers, and the quantity of photoabsorbing agents (ITX) can assist in localizing polymerization to only the desired layer to be cured.

The Folch lab has previously presented SL-based processes whereby high resolution microfluidic devices can be 3D-printed in biocompatible resins based on poly(ethylene glycol) diacrylate (MW ~258) (PEGDA-258), a transparent, cytocompatible polymer featuring low protein adsorption and drug absorption compared to PDMS, and that can sustain cell cultures [13], [18], [19]. The ability to produce small microfluidic channels through photopolymerization depends on the resin's light absorption sensitivity at the printer's wavelength. The absorbance can be quantitatively characterized using the Beer-Lambert law [20], where absorbance (A), defined as the logarithmic ratio between the radiation intensity entering the resin (I_0) and the radiation intensity emerging from it (I), is equal to the product of the radiation path length through the resin (l), the concentration of the absorbing species in the resin (c), and its molar absorptivity (ε):

$$A \equiv \log_{10} \frac{I_0}{I} = \varepsilon l c \qquad \textit{Eq. 1}$$

This relationship directly extends to SL photopolymerization, wherein the depth to which the resin is photopolymerized (z_r) in a vat relates linearly to the logarithm of the exposure time (t_r):

$$z_r = \left(\frac{1}{2.303 \varepsilon c}\right) \times \ln\left(\frac{t_r}{T_0}\right) \qquad \textit{Eq. 2}$$

When applying these principles to SL processes, increasing the absorptivity of the photoresin increases its resolution. Adding more photoinitiator increases the absorptivity of the photoresin and effectively increases the photopolymerization rate, so long as there is an abundance of monomer. However, the drawback to this approach is that increased photoinitiator concentration can disrupt the optical transparency of the generated polymer; for example, yellowing occurs when using excess Omnirad-819 (OM819), a photoinitiator used for non-polar resins. However, adding a photoabsorber - a photosensitizing additive that absorbs light at the printer's emission wavelength but does not participate in the radical polymerization reaction - reduces light penetration through the liquid resin and previously cured polymer allowing the formation of voids and microchannels. Optimizing the relative concentrations of photoinitiator and photoabsorber to monomer enables the creation of unique SL-printed materials that can form microchannels.

Monomer size and composition determine whether hard plastics or hydrogel polymers form from the photopolymerization reaction. Hard plastics are typically the result of low molecular weight monomers forming high-density networks during polymerization. Hard plastics not only form many overlapping covalent bonds within a network, but they also tend to have strong intermolecular interactions between polymer chains, lending them incredible rigidity and molecular impenetrability. Because of their dense molecular packing, hard plastics tend to have high Young's moduli (20-100+ MPa), and they are dry, allowing little to no absorption of solvents [21]. The hard plastic resin formulation used in the Folch lab utilizes the small molecular weight monomer PEGDA-258 in bulk to serve as an organic solvent for the photoinitiator and photoabsorber. Hydrogels are

crosslinked, hydrophilic polymers that do not dissolve in water; instead, they maintain their structure as a colloidal matrix suspended in water. Hydrogels result from the photopolymerization of high molecular weight monomers (PEGDA-6000, for example) dissolved in water forming sparsely packed bonds. Inherent to the high molecular weight of their monomers, hydrogels have gaps between polymer chains which leave space for water to fill, swell, and provide support for the structure of the polymer [22], [23]. Small molecules can travel in and out of the polymer network's pores because hydrogels are hydrated and diffuse. Their Young's modulus depends on 1.) the concentration of monomer suspended within the hydrogel precursor and 2.) the molecular weight of the monomer itself. The photoinitiator and photoabsorber used for hard plastic or hydrogel formation depend on the resin/hydrogel precursor's solvent polarity. Due to the non-polar nature of PEGDA-258 in bulk, our hard plastic resins can only utilize photoinitiators and photoabsorbers that are also non-polar: these include phenylbis(2,4,6-trimethylbenzoyl) phosphine oxide (OM819, formerly known as Irgacure-819, IRG) for our photoinitiator and 2-isopropylthioxanthone (ITX) for our photoabsorber. Hydrogel formulations rely on polar photoinitiators and absorbers, like lithium phenyl-2,4,6-trimethylbenzoylphosphinate (LAP) and tartrazine, respectively. In addition, the UV emission peak of the DLP-SL printer also influences photoresin composition due to the need to maximize absorbance at that given wavelength, most commonly at 385 nm or 405 nm, depending on the printer. The structures of all the molecules described above is shown in Figure 2, as well as a comparison of absorbance profiles of different hard plastic resin formulations against the DLP power spectra of the Asiga Pico 2 HD SL printer. Interchanging these molecular building blocks with materials that have desirable properties or functionality allows for the rapid and tunable creation of new, complex polymers and structures via SL.

a.

	PEGDA hydrogel (MW > 500)	**PEGDA hard plastic (MW = 258)**
Monomer	PEGDA 6k in water 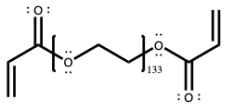	PEGDA 258 in bulk 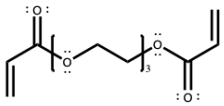
Photoinitiator: Enables polymer formation	LAP – 405 nm 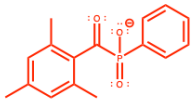	OM819 – 385 nm 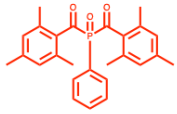
Photoabsorber: Enables microchannel formation	Tartrazine 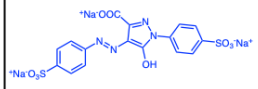	ITX 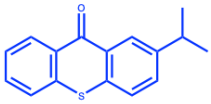
Polymer structure: determined by monomer length 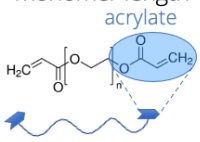	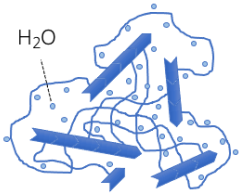	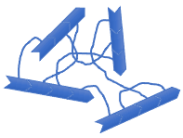
Material properties	➢ Hydrated/Diffusive ➢ Porous ➢ Soft; E=f(M.W.) ➢ Biocompatible	➢ Dry/Impermeable ➢ Densely packed ➢ E=100 MPa ➢ Cytocompatible after post-processing

b.

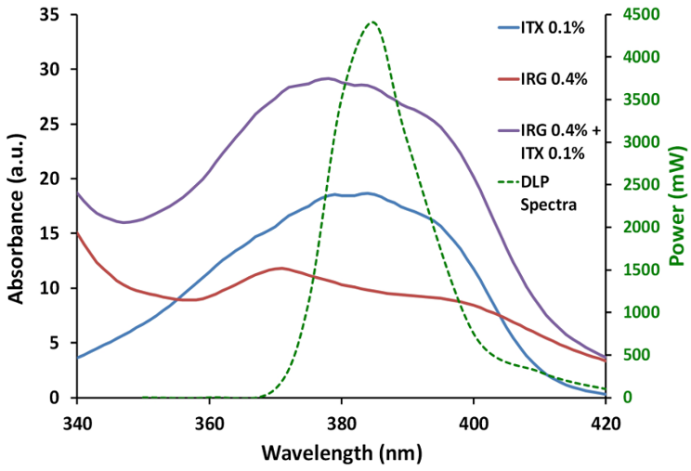

Figure 2: Molecular structures and characteristics of photoresin species. (a.) Structures and properties of plastic and hydrogel polymers, monomers, photoinitiators, and photoabsorbers. (b.) Absorbance spectra of 0.1% ITX, 0.4% IRG (OM819), and 0.4% IRG (OM819) + 0.1% ITX, along with the power spectrum of the UV-LED DLP. The % indicates weight in isopropanol. Graph courtesy of Kuo et. al [19].

Although the monomer backbones may differ depending on the application, the underlying polymerization chemistry remains the same. The photopolymerization reaction mechanism that occurs during SL is shown in Figure 3. Acrylate-functionalized monomers can covalently bond to one another during the radical polymerization reaction, independent of the monomer backbone structure. Thus, resin and hydrogel blends that incorporate multiple types of monomers can be combined to create polymers with new properties determined by the interaction of their constituent parts within the network. For example, Beamish et al. found that by mixing two reactive end-group PEGDA with one reactive end-group poly(ethylene glycol) methyl ether acrylate (PEGMA), the shear modulus of the polymer increased with increasing PEGMA concentration; this is likely because PEGMA reduced the amount of crosslinking within the polymer network, making it more compliant [24]. The ability to selectively change the material properties of SL-printed polymers depending on the application is especially beneficial for biomicrofluidics. The Folch group has already demonstrated that hard plastic resins can be designed to have elastomeric properties and high-resolution print capability in order to produce Quake-style microfluidic valves via SL [25]. These microfluidic valves can be incorporated into a variety of microfluidic automation processes for bioassays or organ-on-a-chips, including routing, timing, and separation of fluids [26], [27]. Furthermore, polymers can be designed to directly affect biological studies by incorporating selective reactive chemistry in the polymer network that immobilizes cell-interacting molecules on the surface of printed constructs. These material advantages, coupled with the semi-automated ability to accurately and reliably produce spatially complex, 3D microfluidic devices, make SL particularly well-suited for the fabrication and rapid prototyping of organ-on-a-chip systems.

The overarching goal of this work was to exhibit the advantages of SL for the production and rapid prototyping of complex microfluidic devices. I will demonstrate this through two main approaches: 1.) the capability of novel, biofunctional SL materials and 2.) intricate microfluidic designs only possible through DM/SL. By proving SL is a valuable tool in the bioengineer's toolbox

for microfluidic device fabrication, testing, and prototyping, I aim to increase the implementation and dissemination of SL as a means of experimenting with more representative *in vitro* biological models.

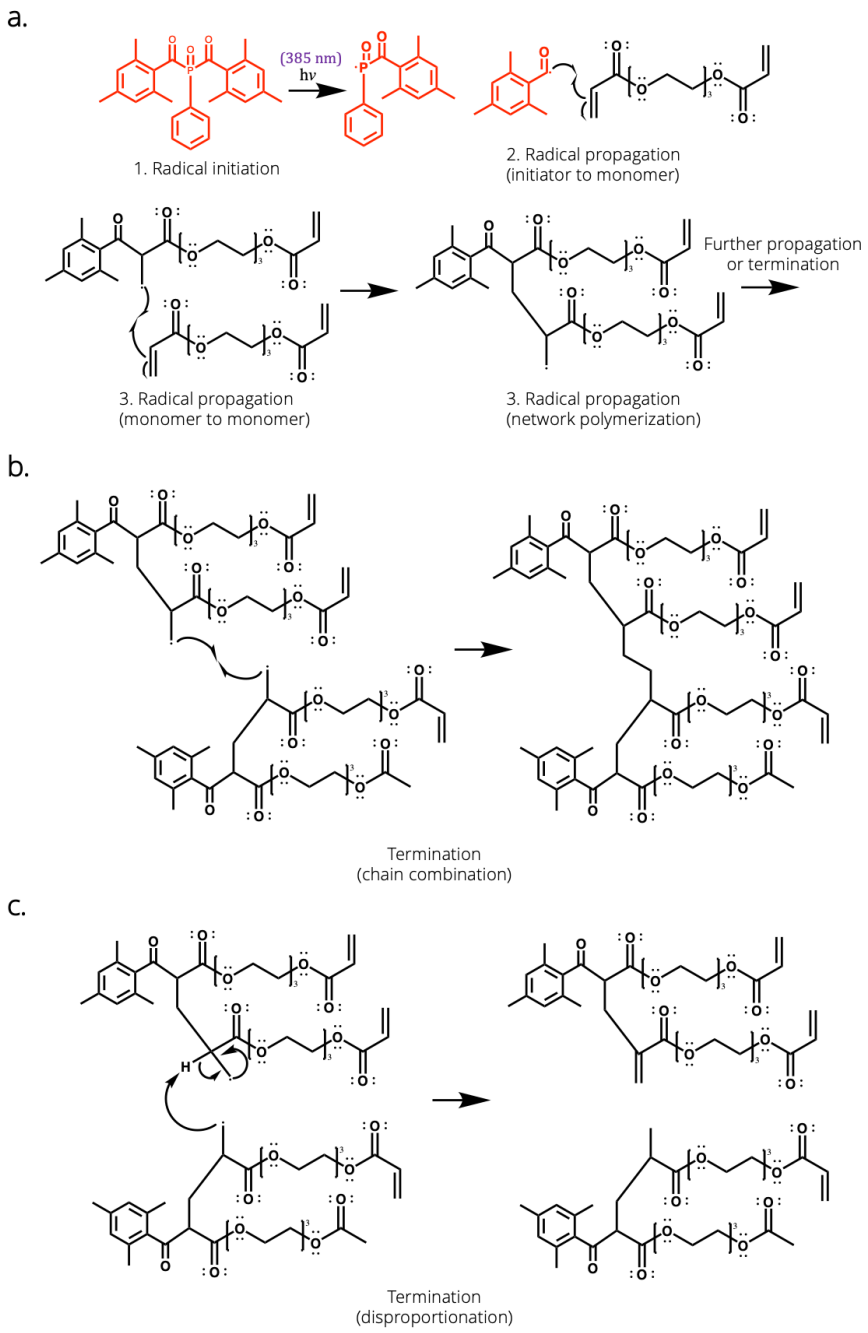

Figure 3: Photopolymerization reaction mechanisms. (a.) Radicals are generated via photolysis from a specific wavelength of radiation. Free radicals attack acrylate end-groups on the monomers, initiating the polymer chain. The polymer chain propagates network bond formation until termination. (b.) Termination by chain combination involves two growing polymer chains reacting with one another to form a single non-reactive polymer chain. (c.) Termination by disproportion involves a hydrogen atom transferring from one radical to the other resulting in two polymer chains, one with a terminal saturated group and the other with a terminal unsaturated group.

2. Functionalization of 3D printed hard plastics

Microfluidic devices and bio-microelectromechanical systems offer a wide range of experimental complexity for biological studies, including the ability to introduce mechanical, electrical, and chemical stimuli to cells in their microenvironment. A fundamental tenet of biomicrofluidics is delivering chemical species such as growth media, cytokines, and drugs through microchannels onto, along, or inside a cell-containing manifold. Although elaborate microchannel design and sophisticated experimental setups can yield unique behavioral outcomes from cells, they fail to effectively investigate substrate effects of biomolecules located on or within 3D microfluidic structures. To conduct these studies, surface engineering techniques must be applied to a device's microchannels during the manufacturing process. Many different surface modification techniques have been developed to address this problem for PDMS devices, including high-energy treatments like plasma or corona to introduce polar functional groups onto the silicone elastomer surface [28], [29]. These processes enable grafting polymers onto the surface, which can, in turn, yield biofunctionality [30]. Although these alternatives exist, they significantly add to the time and complexity of the manufacturing process for PDMS devices, ultimately increasing costs and decreasing fabrication yields. Furthermore, silicone elastomers can regenerate their hydrophobicity over time; thus, permanent functionalization, necessary for long term cell studies, is not reliable [31]. Photopolymeric materials can address these limitations by covalently bonding biofunctional reactive groups to the polymer network.

The Nelson lab has devised two unique monomers that can react with azide- and thiol-functionalized biomolecules. First, Dr. Dylan Karis from the Nelson lab synthesized cyclooctyne methacrylate (COMA, MW=208.30 g/mol), an azide- and acrylate-reactive monomer. COMA is able to functionalize the polymer it is bound to via its cyclooctyne end-group, which spontaneously reacts to azides via strain-promoted azide-alkyne cycloaddition (SPAAC). This reaction is well characterized and has been used in a variety of biochemical applications over the past 60 years [32]. The key

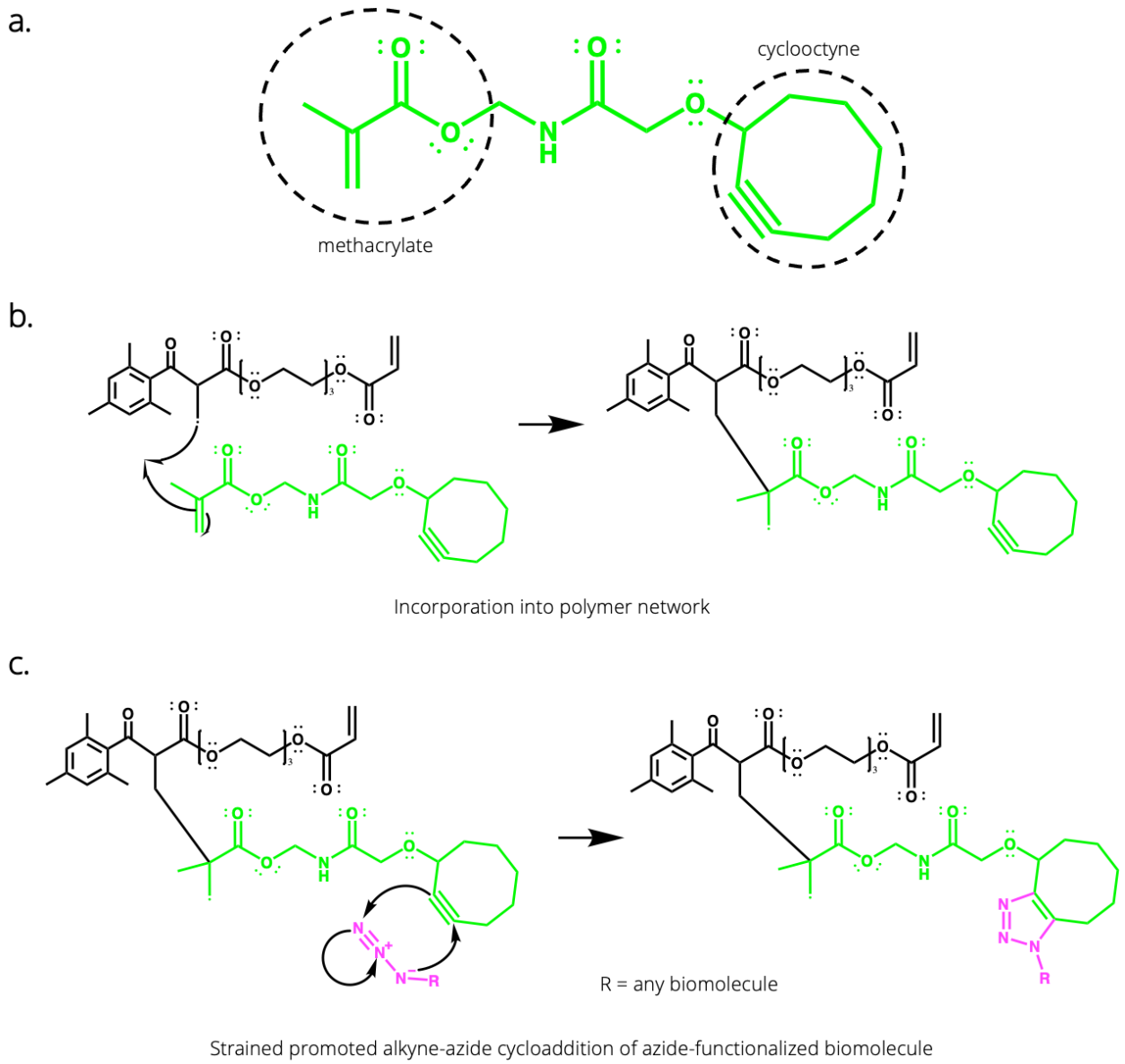

Figure 4: COMA molecular structure and reaction mechanisms. (a.) Molecular structure of cyclooctyne methacrylate. (b.) Mechanism for incorporation of a methacrylate end-group into a polymer network during radical polymerization. (c.) Strain-promoted alkyne-azide cycloaddition (SPAAC) of an azide-functionalized biomolecule, conjugating the polymer network with the biomolecule.

innovation integrates the acrylate-reactive end-group, enabling the monomer to be incorporated into plastic or hydrogel constructs. The molecular structure, integration mechanism into a polymer network, and azide reaction mechanism for COMA are shown in Figure 4. Second, Dr. Christopher Fellin from the Nelson lab synthesized pyridine disulfide urethane methacrylate (PDS-UM, MW=342.44 g/mol), a thiol- and acrylate-reactive monomer. PDS-UM is able to functionalize the polymer it is bound to via its pyridine disulfide end-group, which spontaneously reacts to thiols via

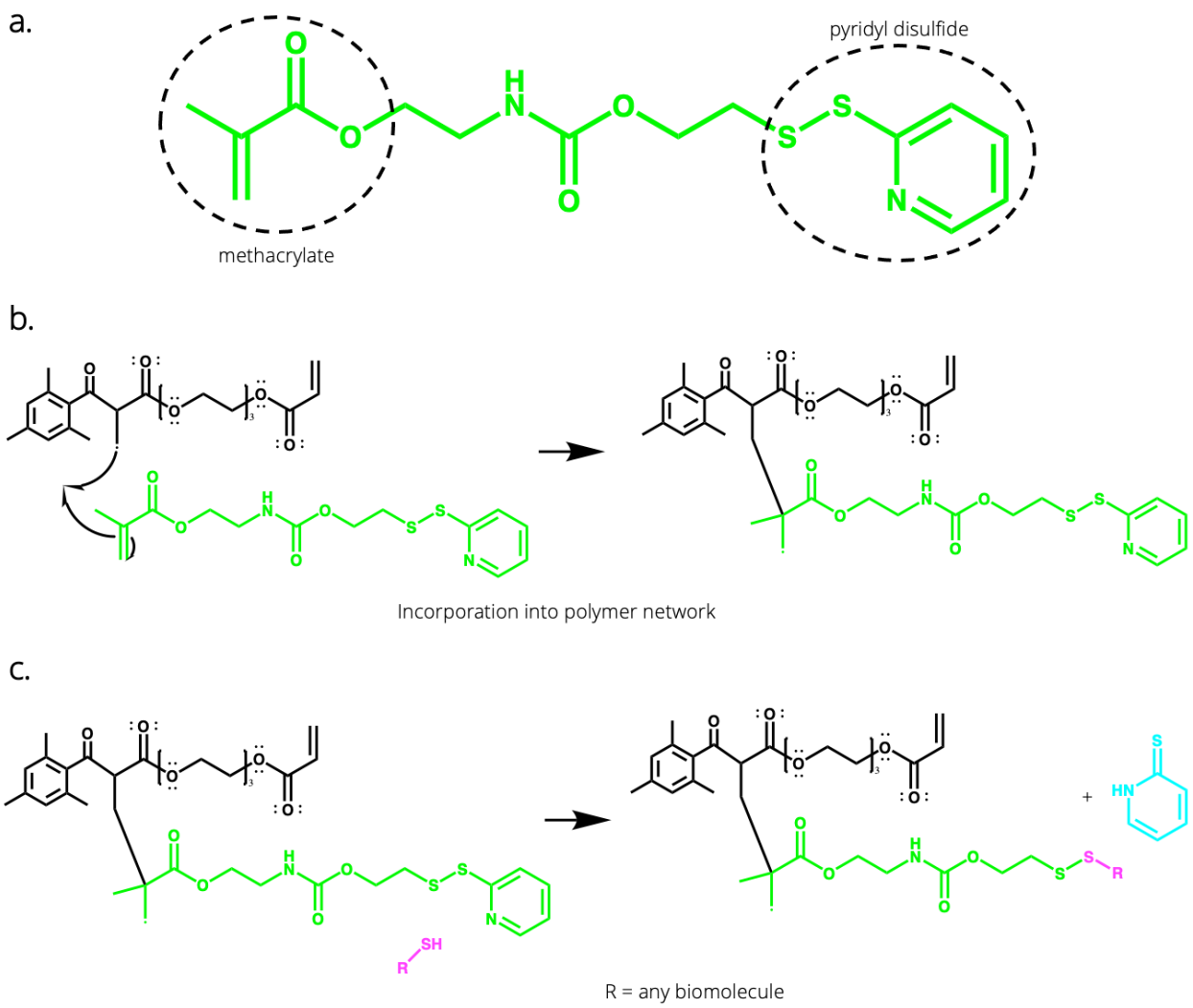

Figure 5: PDS-UM molecular structure and reaction mechanisms. (a.) Molecular structure of pyridyl disulfide urethane methacrylate. (b.) Mechanism for incorporation of a methacrylate end-group into a polymer network during radical polymerization. (c.) Pyridyl disulfide exchange reaction of a thiol-functionalized biomolecule, conjugating the polymer network with the biomolecule and releasing 2-mercaptopyridine.

pyridyl disulfide exchange. This reaction is also well characterized and has been exploited for selective covalent chemistry for many years [33]. Although incorporating the acrylate-reactive end group with pyridyl disulfide has been reported before [34], Dr. Fellin developed a new synthesis scheme which improves yield. The molecular structure, integration mechanism into the polymer network, and thiol reaction mechanism for PDS-UM are shown in Figure 5. By integrating these monomers into the Folch lab's hard plastic resin formulations, I aimed to permanently functionalize the surface of our plastics with any biomolecule of interest via a modular biochemical platform.

Utilizing widely accessible bioconjugation techniques already established for a variety of biochemistry applications, we can use these monomers to create a bioorthogonal bioconjugation platform within printed devices. The bioconjugation scheme is shown in Figure 6. Such a platform would use these monomers to covalently biotinylate the plastic surface and apply biomolecules of interest via bound streptavidin. The working procedure would only consist of reagent washes.

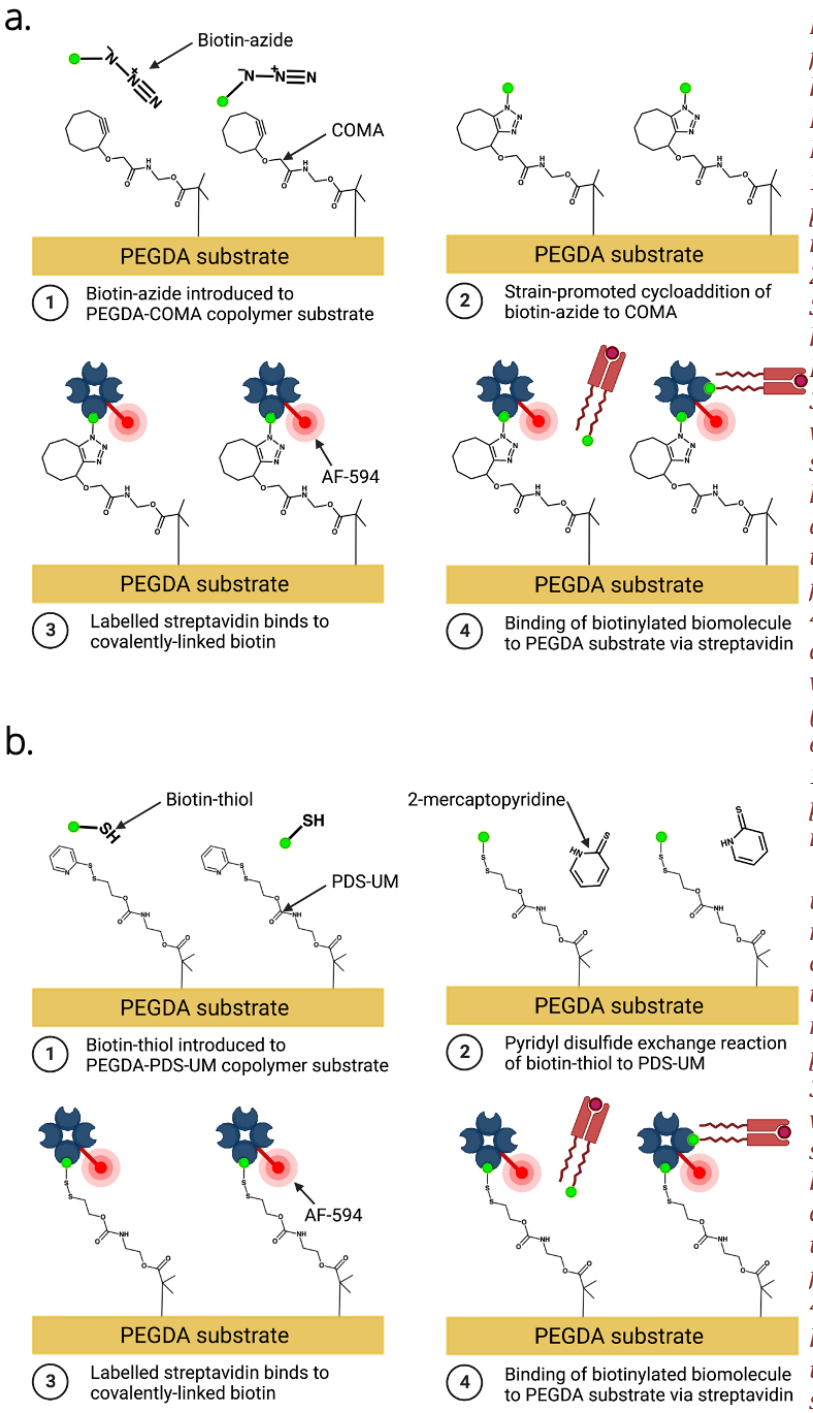

Figure 6: Bioorthogonal functionalization of hard plastics via biofunctional monomers. (a.) Functionalization reaction scheme of PEGDA-COMA copolymer. 1.) PEGDA-COMA copolymer is SL printed, and biotin-azide solution is introduced to the substrate. 2.) Surface presenting COMA undergoes SPAAC with the biotin-azide, covalently biotinylating the surface of the polymer. Excess biotin-azide is washed away. 3.) Fluorescently labelled streptavidin is washed onto the surface of the substrate, binding with high affinity to biotin. Excess streptavidin is washed away. The fluorescent label can be used to validate that the substrate is functionalized with streptavidin. 4.) Open binding sites on streptavidin allow biotinylated biomolecules to bind with the PEGDA substrate. (b.) Functionalization reaction scheme of PEGDA-PDSUM copolymer. 1.) PEGDA-PDS-UM copolymer is SL printed, and biotin-thiol solution is introduced to the substrate. 2.) Surface presenting PDS-UM undergoes pyridyl disulfide exchange reaction with the biotin-thiol, covalently biotinylating the surface of the polymer. The released 2-mercaptopyridine can be measured as a probe to validate biotin conjugation. 3.) Fluorescently labelled streptavidin is washed onto the surface of the substrate, binding with high affinity to biotin. Excess streptavidin is washed away. The fluorescent label can be used to validate that the substrate is functionalized with streptavidin. 4.) Open binding sites on streptavidin bound allow biotinylated biomolecules to bind with high affinity to the PEGDA substrate.

2.1 Methods

To demonstrate the viability of these monomers as a built-in surface functionalization tool, I first needed to determine the resin compositions that would generate an observable signal for surface presentation of the reactive end-group. Beginning with COMA, I tested 1.2 wt% (55 mM) COMA in the standard hard plastic resin: 0.6 wt% OM819 and 0.6 wt% ITX in PEGDA-258 (abbreviated to 0.6/0.6 PEGDA-258 - see Appendix 8.2). The COMA product, synthesized by Claudia Willis from the Nelson lab, came as an oil and was insoluble in water. Dr. Karis had previously shown COMA bonding to a hydrogel network at a working concentration of 0.1 wt% COMA co-solubilized in dimethylsulfoxide (DMSO) in the hydrogel precursor. Because I was using PEGDA-258 in bulk, the monomer acted as an organic solvent allowing COMA to dissolve into the resin. I then created PEGDA-COMA copolymer discs by curing the resin in 5 mm diameter, 1 mm tall PDMS wells. The fabrication and testing protocol is shown in Figure 6a. Initially, I tried to use a fluorescent marker conjugated with an azide to observe functionalization of the azide to the PEGDA-COMA copolymer. The marker I used was fluorescein-azide from Sigma-Aldrich, at a working concentration of 220 μM in DMSO. I compared the fluorescence of the discs before and after treatment with the fluorescein-azide solution by observing them with a Nikon TE3000 epifluorescence microscope at the FITC/GFP wavelength. I then repeated my tests using a 10 wt% (480 mM) COMA solution and changing my conjugation observation scheme. I tried using biotin-azide (Sigma-Aldrich), at a working concentration of 40 μM, and Alexa Fluor 594 (AF594) labeled streptavidin (Thermo Fisher), at a working concentration of 20 μg/mL, to indirectly observe functionalization of the azide to the PEGDA-COMA copolymer. For the biotin-azide/streptavidin-AF594 tests, I pre-treated some of the plastic discs with bovine serum albumin (BSA) to protect against non-specific binding of proteins via adsorption to the polymer surface. I compared the fluorescence of the discs before and after treatment with the biotin-azide/streptavidin-AF594 solutions by observing them with a Nikon TE3000 epifluorescence microscope at the Texas Red wavelength.

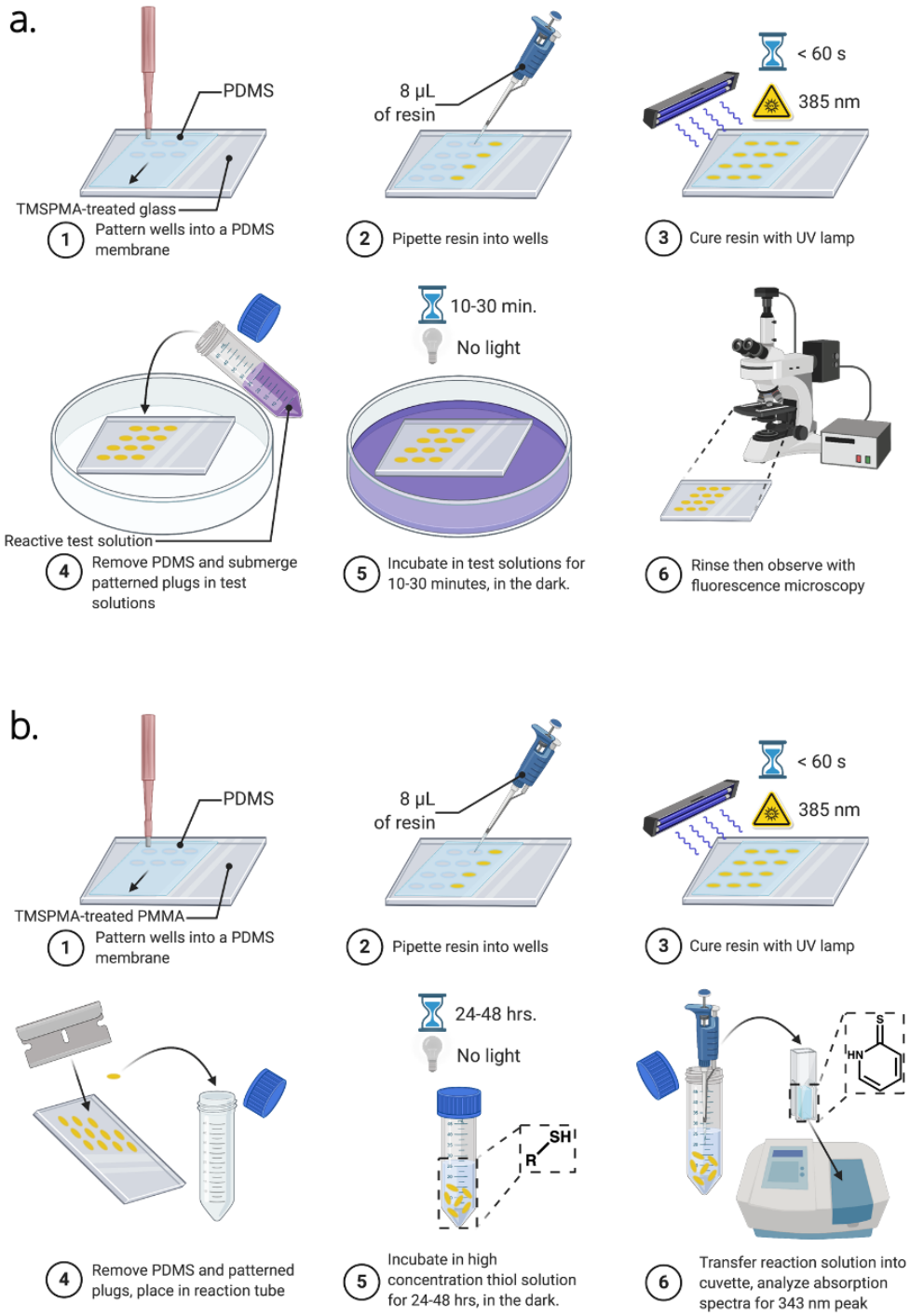

Figure 7: Copolymer fabrication and bioconjugation testing scheme. (a.) Testing for COMA functionalization through fluorescence microscopy. (b.) Testing for PDS-UM functionalization through UV-Vis spectrophotometry.

Leveraging my experience with COMA, I tested 10 wt% (0.292 M) PDS-UM in 0.6/0.6 PEGDA-258. The PDS-UM product, synthesized by Dr. Fellin from the Nelson lab, came as a powder and was insoluble in water. Dr. Fellin had previously shown PDS-UM bonding to a hydrogel network at a

working concentration of 0.06 wt% PDS-UM co-solubilized in methanol (MeOH) in the hydrogel precursor. Because I was using PEGDA-258 in bulk, the monomer acted as an organic solvent allowing PDS-UM to dissolve into the resin. I then created PEGDA-PDS-UM copolymer discs using the same fabrication method as before; however, the testing protocol for this monomer changed, as seen in Figure 6b. Dr. Fellin demonstrated that a 0.06 wt% PDS-UM hydrogel disc (10 mm diameter, 10 mm tall) could react with thiol-containing glutathione (GSH, Sigma-Aldrich) at a concentration of 10 mM in water, releasing enough 2-mercaptopyridine into the reaction solution to be observable by ultraviolet-visible (UV-Vis) spectrophotometry. The release of 2-mercaptopyridine is intrinsic to the conjugation of thiol-containing molecules to PDS-UM. Thus, it serves as a direct observable probe for the efficiency of the conjugation reaction. I prepared six 0.6/0.6 PEGDA-258 control discs and six 10 wt% PDS-UM in 0.6/0.6 PEGDA-258 treatment discs, incubating them separately for 48 hours in 2 mL of 150 mM GSH in water. After, I removed the discs, diluted the reaction solutions down to 30%, 10%, and 1% to a final volume of 3 mL in water, and performed UV-Vis spectrophotometry.

2.2 Results and discussion

The COMA experiments failed to demonstrate that cyclooctyne was on the plastic surface and was able to form bonds with azide-functionalized biomolecules. The results of these experiments are shown in Figure 7. Comparing the fluorescence of 1 wt% COMA in 0.6/0.6 PEGDA-258 to that of the control before and after fluorescein-azide treatment reveals no statistical difference between measurements taken along the edge of the disc nor in the center. Similarly, tests with biotin-azide/streptavidin-AF594 failed to show any significant difference between control and treatment discs and test solutions. The experimental approach for COMA was fundamentally flawed because of three main factors: 1.) Viewing slight changes in fluorescent signal due to surface functionalization is obfuscated by the inherent thickness of the disc being observed, where the vast majority of fluorescent signal comes from light shining through the non-accessible/non-conjugated internal

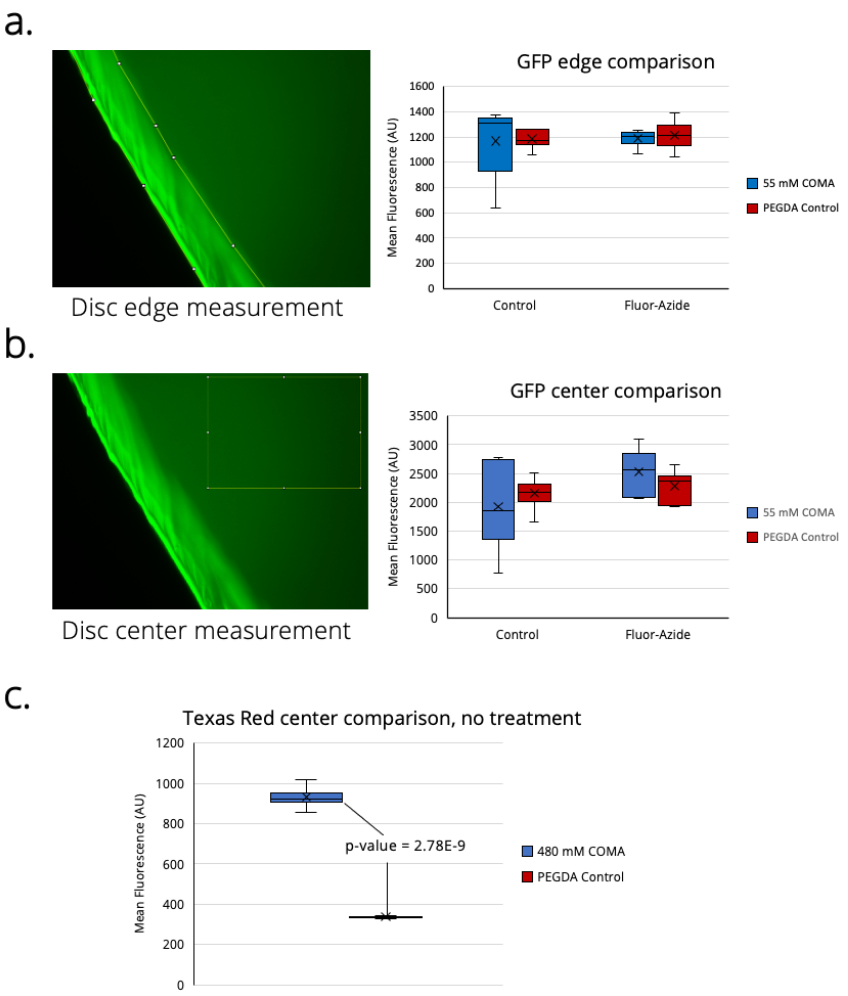

Figure 8: COMA fluorescence results. (a.) Disc edge GFP fluorescence comparison of 55 mM COMA in 0.6/0.6 PEGDA-258 treatment and 0.6/0.6 PEGDA-258 control reveals no statistical difference between treatment and control discs before or after treatment with 220 µM fluorescein-azide solution. (b.) Disc center GFP fluorescence comparison of 55 mM COMA in 0.6/0.6 PEGDA-258 treatment and 0.6/0.6 PEGDA-258 control reveals no statistical difference between treatment and control discs before or after treatment with 220 µM fluorescein-azide solution. (c.) Disc center Texas Red fluorescence comparison of 480 mM COMA in 0.6/0.6 PEGDA-258 treatment and 0.6/0.6 PEGDA-258 control reveals a statistically significant difference between treatment and control discs before any reactive solutions are introduced. This indicates that COMA in PEGDA has background fluorescence at 594 nm wavelength.

volume of the disc rather than its exterior surface, 2.) 0.6/0.6 PEGDA-258 control has background fluorescence on the FITC/GFP wavelength, and 10 wt% COMA in 0.6/0.6 PEGDA-258 has significant background fluorescence on the Texas Red wavelength compared to that of the 0.6/0.6 PEGDA-258 control - both confound signal gains, and 3.) changes in fluorescence may be attributed to protein adsorption, whereby proteins non-specifically bind to the plastic surface, confounding the fluorescence reading meant to measure how much covalent bonding is occurring. These limitations

are related to fluorescence microscopy not being a sensitive enough detection method to differentiate signal changes from surface-level molecular reactions that may only involve picomolar amounts of reactive molecules. For this reason, further tests should be done utilizing a detection method like that of PDS-UM, where a molecular probe related directly to successful conjugation can be observed via spectrophotometry. This type of molecular signaling scheme guarantees that slight signal changes are detected with high sensitivity and are only associated with the concentration of reacted molecules on the hard plastic surface.

It is also possible that the cyclooctyne itself may have been defective, leading to these null results. This hypothesis stems from the fact that the 10 wt% COMA in 0.6/0.6 PEGDA-258 treatment disc had a significant amount of background fluorescence in the Texas Red wavelength compared to the 0.6/0.6 PEGDA-258 control disc, even though cyclooctyne should not be fluorescent. The implication is that the photopolymerization process transformed the structure of cyclooctyne, rendering it unable to participate in the SPAAC reaction. To test this hypothesis, several analysis techniques are being applied to our COMA synthesis product and our COMA copolymer discs. First, nuclear magnetic resonance spectroscopy (NMR) is being done on the COMA oil we received from Claudia Willis to determine if the monomer has changed structure while it has been stored since synthesis, or if any contaminants are present that may inhibit SPAAC. In addition, the 10 wt% COMA in 0.6/0.6 PEGDA-258 treatment discs and their 0.6/0.6 PEGDA-258 control discs are being compared via infrared red (IR) spectroscopy to reveal if alkyne groups are present in the polymeric sample. With further validation of our molecular system and a different bioconjugation validation approach the Folch lab can continue to explore COMA as a possible method for creating a modular bioconjugation platform on SL printed plastics.

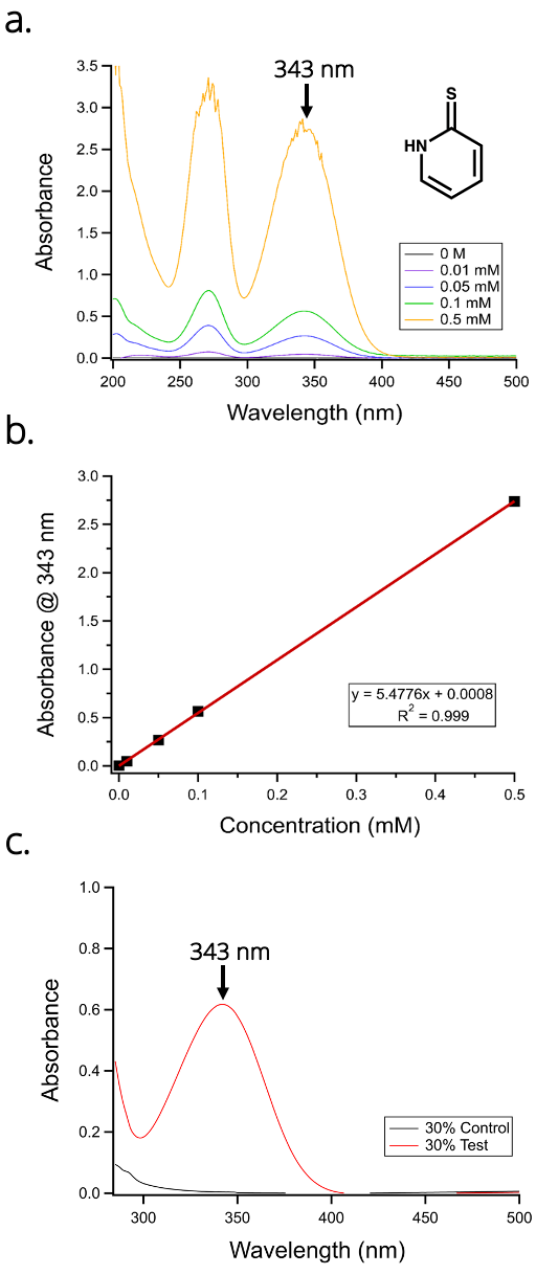

Figure 9: PDS-UM UV-Vis spectrophotometry results. (a.) The absorption spectra of 2-mercaptopyridine at various concentrations in solution. 2-mercaptopyridine has a distinct absorption peak at 343 nm which can be a useful reference point for determining its quantity in solution. (b.) The calibration curve of 2-mercaptopyridine based off its absorbance at the 343 nm wavelength, correlating concentration to absorbance via Beer's law (see Eq. 1). (c.) The absorbance spectrum of the 30% diluted test solution of six 10 wt% PDS-UM in 0.6/0.6 PEGDA-258 treatment discs in 150 mM of GSH compared to that of control treatment discs. The 30% diluted test solution had an absorbance peak of 0.617 at the 343 nm wavelength which corresponds to the same absorbance curve and peak expected from 2-mercaptopyridine. The 10% and 1% diluted samples did not show any absorbance difference between control and test treatments, indicating that the spectrophotometer was not sensitive enough to detect that low of concentration of 2-mercaptopyridine in solution. All absorbance measurements and graphs were provided by courtesy of Dr. Christopher Fellin from the Nelson lab.

The PDS-UM experiment reveals that 10 wt% PDS-UM in 0.6/0.6 PEGDA-258 is on the surface of the cured hard plastic disc and can undergo pyridyl disulfide exchange with free-floating GSH in solution. The results of this experiment are shown in Figure 8. The pyridyl disulfide exchange releases 2-mercaptopyridine as a byproduct of PDS-UM bioconjugation with a thiolated molecule. This byproduct, when released back into the test solution, has a distinct absorbance curve which can be used to quantify the concentration of PDS-UM that had undergone the disulfide exchange reaction. Dr. Christopher Fellin provided the absorption spectra of 2-mercaptopyridine at various

concentrations in solution, which revealed an absorption peak at 343 nm wavelength. These spectra were used to create a calibration curve that correlated absorption at 343 nm wavelength to concentration of 2-mercaptopyridine in solution. Then, by measuring the absorption spectra of the test and control disc treatment solutions after incubation, the concentration of 2-mercaptopyridine present in solution could be back-calculated using the calibration curve. I diluted the test and control disc treatment solutions down to 30%, 10%, and 1% of the original concentration to ensure that the concentration of 2-mercaptopyridine that may or may not be present in solution would fall within the detection range of the spectrophotometer being used. The 30% diluted test disc treatment solution had an absorption peak of 0.617 at the 343 nm wavelength, corresponding to a concentration of 0.113 mM 2-mercaptopyridine in solution, whereas the 30% diluted control disc treatment solution had ~0 absorbance at that wavelength. This implies that the original test disc treatment solution had a concentration of 0.377 mM 2-mercaptopyridine; the treatment solution had a total volume of 2 mL, therefore, 7.53E-7 moles of 2-mercaptopyridine were present after 48 hours of incubation in 150 mM GSH. Because 2-mercaptopyridine is only present in solution as a byproduct of the disulfide exchange reaction, it can be used to calculate the conjugation efficiency of 10 wt% PDS-UM in 0.6/0.6 PEGDA-258.

The PDS-UM test discs were made from 8 μL/disc of 0.292 M PDS-UM in 0.6/0.6 PEGDA-258 resin. There were 6 discs present in each treatment solution, therefore, there was 1.4E-5 moles of PDS-UM total in the hard plastic test discs. Calculating the percentage of 2-mercaptopyridine present with the total amount of PDS-UM (7.53E-7 moles/1.4E-5 moles) shows that 5.38% of the total PDS-UM reacted with GSH. Although this seems like low efficiency, this is because PEGDA-258 hard plastics have very little penetration of molecules into the polymer bulk. The majority of PDS-UM reacting can be assumed to be only on the surface of PDS-UM discs and not in the disc volume. The disc had a radius of 2.5E-3 m and height of 1E-4 m, so the surface area of the disc was 4.08E-5 m^2. Assuming that the accessible surface of the disc is 10 nm deep in size, then the total accessible volume

is 4.08E-13 m^3. If 10% of that volume was PDS-UM, because of the 10 wt% present in the resin mixture, then 4.08E-14 m^3, or 4.08E-11 L, of PDS-UM was accessible for reaction. At 0.292 M PDS-UM, this means that only 1.19E-11 moles of PDS-UM were accessible per disc, and therefore 7.15E-11 moles of PDS-UM were accessible across 6 discs. This only accounts for 0.0095% of the total 2-mercaptopyridine released into solution. This analysis has two possible implications: 1.) the amount of accessible PDS-UM reactive in the polymer network is greater than assumed, or 2.) there is a substantial amount of unreacted PDS-UM, not incorporated into the polymer network, that is on the copolymer disc. In order to gain greater insight into the nature of the PDS-UM copolymer, further tests should be conducted that more thoroughly test the conditions of the PDS-UM disc. For example, a repeat experiment should be conducted that thoroughly washes the copolymerized disc with MeOH before incubation in the GSH solution. Performing this extra treatment step could remove any unpolymerized PDS-UM that may be reacting with GSH. Alternatively, a different experiment could compare the PDS-UM conjugation efficiency of objects with different total surface areas but the same total volume. This would help to analyze the effect of accessible surface area on conjugation efficiency. All-in-all, these tests have yielded promising results that have many exciting implications for the creation of a modular bioconjugation platform.

3. Developing a materials testing platform for stereolithography

As new monomers are developed that introduce novel functionality to microfluidic structures, printing those materials remain limited by the architecture of most commercial SL printers. Like those made by the Nelson lab, custom monomers often involve many synthesis, processing, and purification steps which require significant time and labor investments, increasing the cost/gram of monomer [35]. Synthesis yields are often low (< 20%) depending on the monomer's chemical make-up and complexity. Thus, synthesized monomers are limited in quantity and must be used sparingly in order to maximize the number of prints produced with them. Most commercial SL printers aim to maximize the possible build area upon which high-resolution structures can be built. This is advantageous for microfluidic purposes as increasingly large microfluidic arrays can be fabricated via SL, improving the complexity and functionality of a single chip. However, this feature is detrimental for material prototyping purposes as SL printing requires a uniformly distributed, 5 mm thick (minimum), liquid resin/hydrogel precursor to cover the entirety of the build area. For commercial printers like the Asiga Pico 2 HD, with a 52 mm x 29 mm build area, or the Elegoo Mars Pro, with a 120 mm x 68 mm build area, the minimum volume of resin is as high as 30 mL. The amount of monomer available to print with becomes prohibitive when utilizing resin compositions that have high weight percentages of monomer (> 1 wt.%). This limits the ability to test experimental monomers with SL, often requiring repeated troubleshooting and optimization trials to get a satisfactory device. Therefore, there is a need to maintain the high-resolution printing ability of SL printers with a low build area/volume.

To address the prohibitive size of commercial SL build areas for experimental monomers, I have designed and developed a custom build plate and resin vat for the Elegoo Mars Pro that will allow printing with resin volumes as low as 5 mL. The Elegoo Mars Pro is ideal for modification as it is reasonably priced at $200 USD, and it has widely available, low-cost replacement parts for repair if printer alterations lead to damages. A schematic of the printer's modifications is shown in Figure

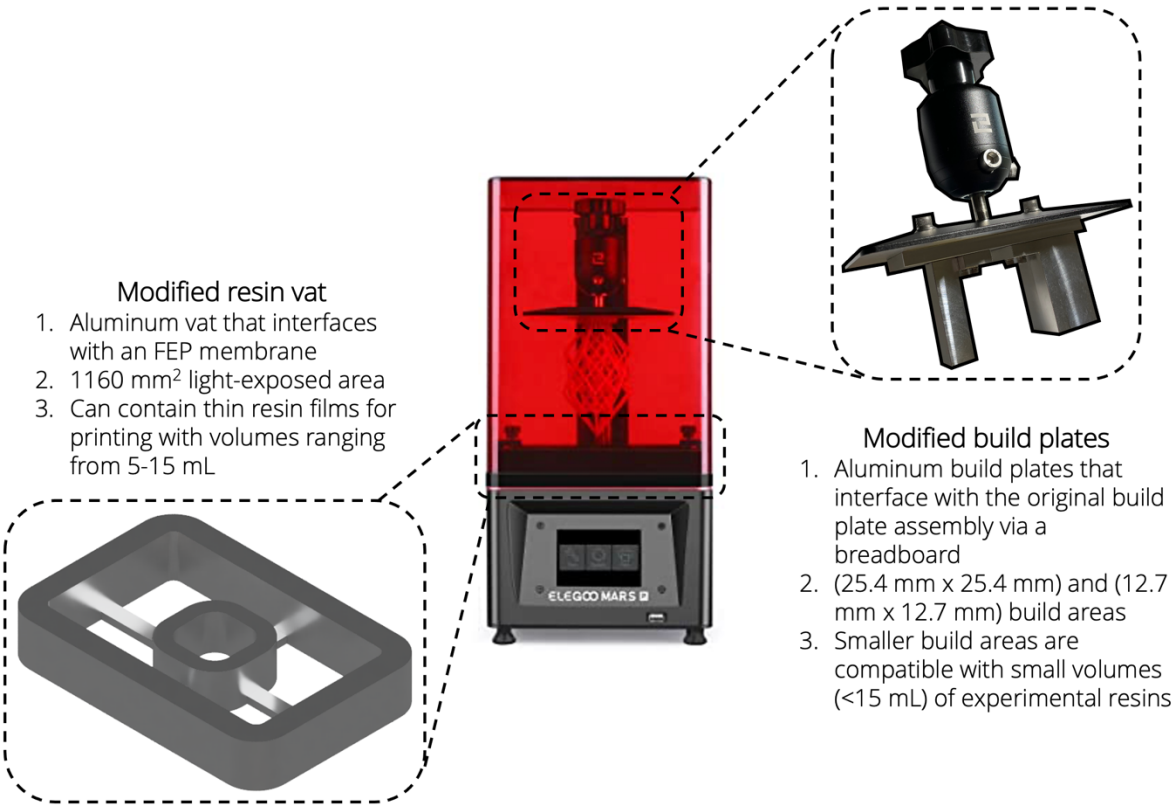

Figure 10: Elegoo Mars Pro SL printer modifications. The custom-made build plate and resin vat assembly allow for printing with resin compositions as low as 5 mL, enabling SL experimentation with new monomers.

10. The custom build plates were designed to interface with the original build plate because of its built-in rotatory knob connection to the z-axis stepper motor. The custom build plates screw into a breadboard that is attached to the original build plate via screws. The breadboard was designed to have evenly spaced screw holes throughout the plate to allow for customizable positioning of one or more custom build plates along the light-exposed area of the original vat. The modified resin vat limits the resin volume to 5-15 mL at the center of the UV-LED array. The modified resin vat has the same mechanism for FEP membrane attachment as the original resin vat. The custom build plates were fabricated in aluminum by Gregory Anderson from the Washington National Primate Research Center (WaNPRC). The custom resin vat is still in the process of being fabricated.

Although the modified Elegoo Mars Pro is ideal for testing experimental resin compositions, the main drawback is the UV-LED array's 405 nm wavelength, which substantially decreases the efficiency of photopolymerization and microchannel creation for our most used resin, 0.6/0.6

PEGDA-258. When printing with the Asiga Pico 2 HD, which has a 385 nm UV-LED array, the 0.6/0.6 PEGDA-258 resin can produce microchannels with diameters as small as 108 μm. On the Elegoo Mars Pro, the 0.6/0.6 PEGDA-258 formulation struggles to produce channels with a diameter smaller than 2 mm. There are two main approaches for improving SL printing resolution: 1.) optimizing print parameters, and 2.) modifying resin formulations. Changing print parameters allow some flexibility in the outcome of the polymeric material; the most important settings are the UV-LED exposure time and layer height. For microchannel formation, the goal is to minimize the exposure time for a given layer height to prevent microchannel occlusion by over-exposure of previously polymerized layers; it is also vital to ensure that the resin in that layer height is completely polymerized after exposure. The Folch lab has already identified the best settings for printing 0.6/0.6 PEGDA-258 on the Asiga Pico 2 HD based off previous work. However, the UV-LED array wavelength difference between the Asiga Pico 2 HD and Elegoo Mars Pro means that the photopolymerization-related print settings are not directly translatable. Thus, I characterized and optimized the print settings for a 50 μm layer height of 0.6/0.6 PEGDA-258 on the Elegoo Mars Pro through a series of test prints. The print settings for 0.6/0.6 PEGDA-258 on the Asiga Pico 2 HD and Elegoo Mars Pro are shown in Table 1. Tuning these parameters can help optimize device fabrication, but there is a fundamental limit to the resin's photopolymerization capability, given the printer's UV-LED wavelength. Therefore, it is necessary to modify the resin composition when certain features cannot be produced with print parameter changes. To this end, I kept the Elegoo Mars Pro print settings constant while increasing the concentration of photoabsorber when trying to produce 1 mm diameter channels. The results of this resin optimization effort are shown in Figure 11. The printer's resolution gradually improved with increasing concentrations of ITX, eventually resulting in 1.2 mm diameter microchannel formation. The resolution of hard plastic printing on the Elegoo Mars Pro can be further enhanced by using a resin formulation that includes a photoinitiator and photoabsorber with an absorption peak at or near 405 nm wavelength.

	Asiga Pico 2 HD			Elegoo Mars Pro
Print setting	10 um layer	25 um layer	50 um layer	50 um layer
Exposure time (s):	0.15-0.20	0.2-0.3	0.5-0.8	4-6
Burn-in exposure time (s):	2	4	6	30
Light intensity (mW/cm^2):	85.00			N/A
Separation velocity (mm/s):	0.16			2.5
Separation distance (mm):	2			5
Wait time (after exposure) (s):	6			6

Table 1: SL print settings for 0.6 wt.% OM819 and 0.6 wt.% ITX in PEGDA-258 on the Asiga Pico 2 HD and Elegoo Mars Pro.

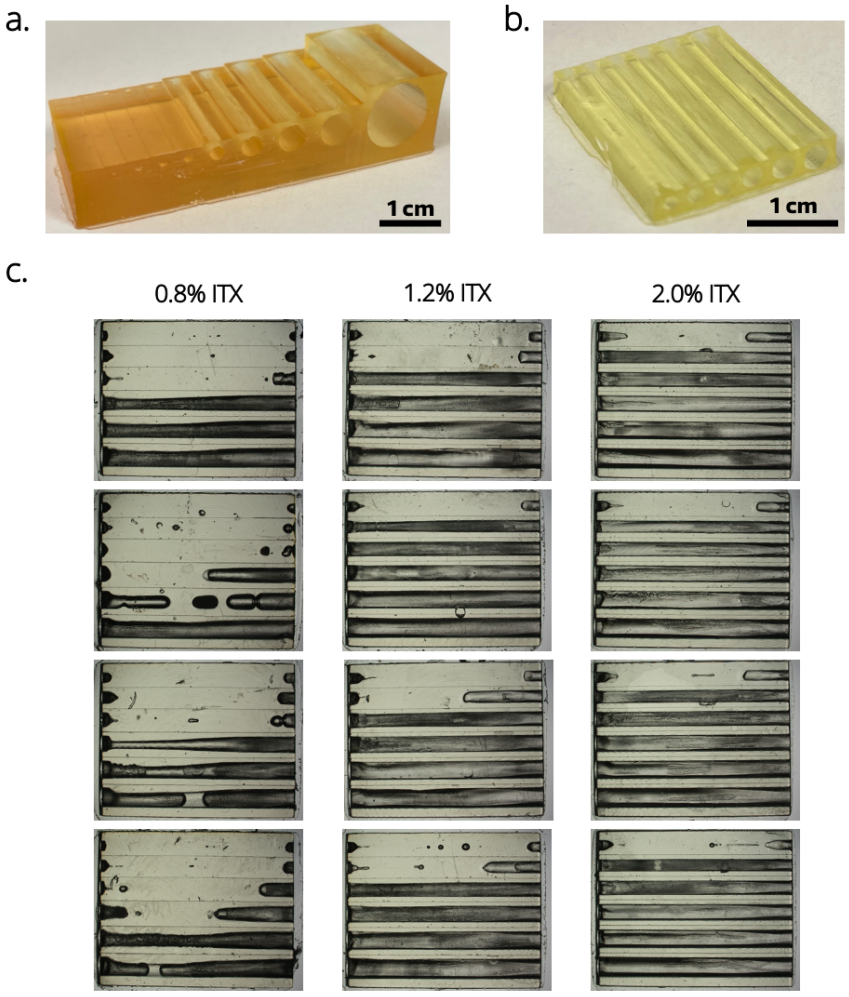

Figure 11: Hard plastic resin optimization for the Elegoo Mars Pro. (a.) Microchannel test print of 0.6 wt.% OM819 and 0.6 wt.% ITX in PEGDA-258 using a 4.5 second exposure time and 50 µm layer height. Channels are 20 mm long with a 1 mm thick roof. Diameters (mm) from right to left: 10, 5, 4, 3, 2, 1, 0.8, 0.6, 0.4, 0.2. (b.) Microchannel test print of 0.6 wt.% OM819 and 2.0 wt.% ITX in PEGDA-258 using a 4.5 second exposure time and 50 µm layer height. Channels are 20 mm long with a 1 mm thick roof. Diameters (mm) from right to left: 2.0, 1.8, 1.6, 1.4, 1.2, 1.0. (c.) Microchannel test prints of the same model from (b.), with varying concentrations of ITX. Diameters (mm) from bottom to top: 2.0, 1.8, 1.6, 1.4, 1.2, 1.0.

4. Accounting for material constraints through device design

When implementing SL to the creation of physiologically representative muscle models, several crucial needs must be met. The most fundamental function of a muscle model platform is that it must be able to culture and differentiate myoblasts and myocytes within it. Progenitor cell culture requires precise temporal and spatial control of nutrient gradients, and as such, extensive structural and material design considerations must be made to accommodate those conditions. Progenitor cell differentiation often requires culturing over long time scales (e.g. 7-28 days), which is only possible if the material the cells are cultured in/on is biocompatible. Furthermore, cell viability depends on readily available exchange methods for gases, nutrients, and cellular waste products. These biotransport methods could take the form of molecular diffusion through the matrix suspending the cells or convective fluid flow in channels adjacent to the cell culture chamber. However, they must be regulated not to harm the cells by nutrient saturation or starvation. We aimed to reproduce the well-documented micropatterning, culture, and subsequent differentiation of myoblast-in-gel to myocyte to myotube within an SL printed device [36]–[38].

The formation of myotubes depends strongly on the extracellular matrix in which the myoblast, and derived myocytes, are suspended. In work that was never published, the Folch lab observed that when a suspension of C2C12 myoblasts in collagen gel precursor is injected into a microchannel, myotube fusion is observed parallel to flow presumably due to guidance by the collagen fibers. This effect has also been observed in bio-printed, cell-laden hydrogels, where the same effect noted above occurs from extrusion through the bioprinter's nozzle [39]. The cell culture chamber must be able to flow gel precursor with high viscosity and high surface tension and allow the diffusion of cell culture media. PDMS's gas permeability allows gas exchange to occur through the walls of a microfluidic device, but hard plastic devices must be intentionally designed with features that allow for gas exchange. Here I will exhibit an SL printed, microfluidic device that incorporates microchannels for cell-in-gel patterning and fenestrations for gas and nutrient exchange.

4.1 Methods

The SL printed, microfluidic, cell culture device was designed to have three main features:

1.) a cell culture chamber with an aspect ratio small enough that when a gel precursor flows through it, microfluidic shear forces the alignment of collagen fibers
2.) fenestrations that interfaced with the cell culture chamber to allow gas and nutrient exchange but were restrictive in dimension to prevent a high surface tension gel from escaping
3.) a cell media well to contain and supply the cell culture chamber with oxygen and nutrients.

After testing several iterations of different channel sizes and fenestration configurations, I settled on the schematic shown in Figure 12. The device was fabricated with the Asiga Pico 2 HD in 0.6/0.6 PEGDA-258 using the 50 μm layer height settings shown in Table 1. In addition to the device, two control treatments were also tested: 1.) cells-in-gel extruded onto an SL printed, 0.6/0.6 PEGDA-258 well, and 2.) cells-in-gel extruded onto a tissue-culture treated well. Prior to cell culture, the SL printed plastics were gravity-rinsed with DI water for 48 hours to remove toxic leachates, then UV-treated for 24 hours, trapping any remaining leachates in the polymer network and sterilizing the devices. C2C12 cells were prepared by staining 50% of cells with 20 μM CellTracker-Green (Thermo Fisher) and 50% of cells with 20 μM CellTracker-Orange (Thermo Fisher). The labeled cells were then mixed into a gel precursor containing 1.6 mg/mL Collagen Type-1 Rat tail (Corning) and 1:6 by volume Matrigel matrix (Corning) at a cell concentration of 2E6 cells/mL. The cell-containing gel solution was then loaded into the device through the fluidic connectors via a slip-seal syringe. The cells were cultured in high-glucose Dulbecco's Modified Eagle Medium (DMEM, Thermo Fisher) supplemented with 10 vol.% fetal bovine serum (FBS, Hyclone), and grown in a 5% CO_2 atmosphere at 37 °C and 100% humidity. The entire device and controls were kept covered and contained within a humidified Petri dish to prevent evaporation. The media was replaced every 24 hours. After 3 days

of culture, the cells were observed with a Nikon TE3000 epifluorescence microscope at brightfield, FITC/GFP, and Texas Red wavelengths.

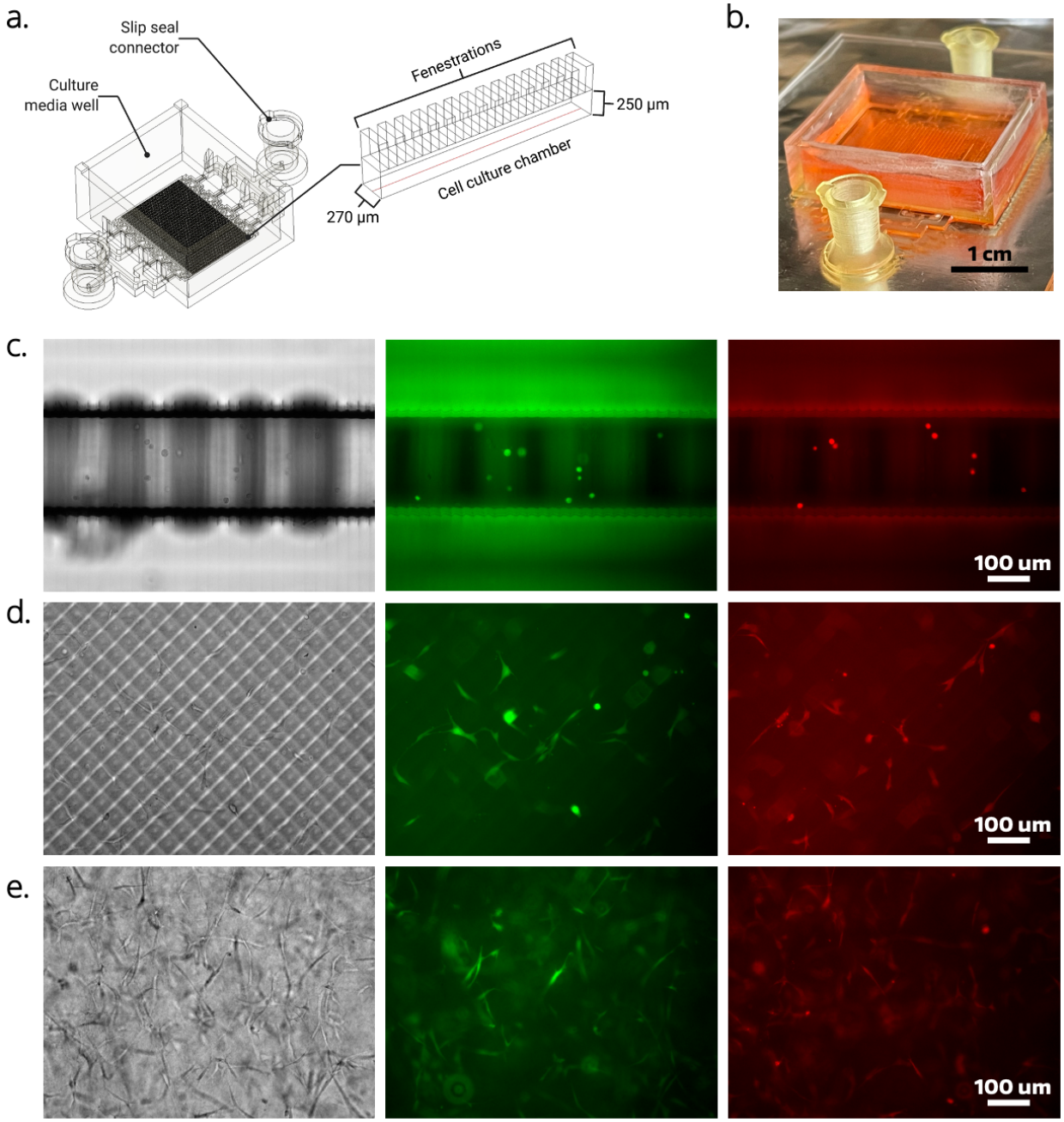

Figure 12: C2C12-in-gel micropatterning and culture in an SL printed device. (a.) Microfluidic device schematic for gel patterning and cell culture. (b.) Image of the device loaded with cell culture media. (c.) Brightfield (left), FITC/GFP (middle), and Texas Red (right) fluorescent images taken of cell-in-gel cultures after 3 days within the SL printed microfluidic device. (d.) Brightfield (left), FITC/GFP (middle), and Texas Red (right) fluorescent images taken of cell-in-gel cultures after 3 days on a SL printed culture well. (e.) Brightfield (left), FITC/GFP (middle), and Texas Red (right) fluorescent images taken of cell-in-gel cultures after 3 days on a tissue-culture treated culture well.

4.2 Results and discussion

After three days of culture within the microfluidic device, the C2C12 cells were still unable to spread, migrate, or proliferate. The PEGDA-258 and tissue culture treated well conditions showed much healthier C2C12's as evidenced by the spreading, proliferation, and joining of cells while in the gel matrix. The most rapid proliferation, and what can be presumed as healthiest population of cells, was that of the tissue culture treated well. This is likely because the PEGDA-258 hard plastic was still leaching cytotoxic leachates, which reduced the proliferability of cells within their microenvironment. The cells in the PEGDA-258 culture well showed signs of spreading and proliferation because the toxic leachates were diluted in the large volume of media contained within the well. However, the cells in the microfluidic device were not readily accessible to the culture media, instead being surrounded by PEGDA-258 substrate. After 5 days of continued exposure to leachates in the microenvironment, the C2C12's within the device died. The goal of this experiment was to continue the culture until C2C12 fusion, whereby the CellTracker-Green labelled cells and CellTracker-Orange labelled cells would fuse yielding a yellow color in the composite fluorescent image. However, by day five, all C2C12 cells within the device had died, the PEGDA-258 well had broken and started leaking cell culture media, and clumps of cells-in-gel in the tissue culture treated well started separating from the bottom of the well and floating in the media. All these factors made it impractical to continue the experiment so it was halted before differentiation and fusion could be observed.

Many different procedural and device changes should be explored to improve the outcome of this experiment. First, changing the resin composition to minimize the amount of photoinitiator and photoabsorber can help to reduce the effect of toxic leachates on cell culture. The 0.6 wt.% of OM819 and ITX was chosen for its ability to produce high-resolution features, but that high concentration may not be necessary to produce this specific device. Second, the post-processing procedures used to remove toxic leachates can be further optimized to accomplish their goal more effectively.

Alternatives include longer rinses of microfluidic channels with solvents, higher flow rates to induce more mass transport of chelate along the substrate, utilizing different solvents such as isopropanol or acetone that can more effectively solvate PEGDA, and treating the surface with biocompatible proteins to help buffer the effect of the substrate on the cells culturing on it. While the initial results from this experiment were discouraging, there is a newfound opportunity to improve the approach for using SL printed devices for long-term cell cultures.

5. Developing 3D spatiotemporal gradients with digital manufacturing

Biomolecular concentration gradients are ubiquitous in all living organisms and are quintessential to development. Although gradients are known to play a vital role in cell migration, differentiation, angiogenesis, and homeostasis *in vivo*, studies into how these gradients affect cellular constructs like organs have been limited by the ability to reliably produce large-scale (> 1 mm) gradients *in vitro* [40]. Advances in microfluidics have enabled the creation of devices that rapidly establish non-linear, continuous flow-based gradients on a large scale [41]. These developments have revealed several new biological insights into chemotaxis, sprouting, and more [42], [43]. While flow-based gradients are advantageous for precisely controlling the steady-state delivery of a gradient, two key drawbacks limit their application for the study of broader biological phenomena: 1.) flow occurs directly onto cells producing shear stress on them which could disrupt or confound the biological process under study and 2.) cell signaling molecules are continually washed away which prevents the investigation of cellular interactions in response to a given gradient condition. Diffusion-based gradients address these limitations by utilizing passive diffusion to establish a gradient from a source to a sink in a convection-free environment. However, establishing such gradients *in vitro* has been challenging because of the impractical time scales required to establish steady-state diffusive gradients across a large volume. Based on a concept by Dr. Nirveek Bhattacharjee from the Folch lab, a tunable spatiotemporal gradient generating platform has been devised that can generate complex, 3D, steady-state gradients in very short time scales (< 3 hours).

Manufacturing microfluidic devices with SL has fixed fabrication constraints associated with the printers and resins used to create the device. For example, the Asiga Pico 2 HD is equipped with a 1,080 pixel, 385 nm UV-light, high definition projector (1,920 x 1,080 pixels), which results in a projected pixel width of 27 um in XY over an area of 52 mm x 29 mm. Theoretically, this means that minimum feature sizes are 27 um x 27 um, but because of the practical limitations associated with photopolymerization, the minimum feature size is closer to 81 um x 81 um. Furthermore, the build

area constrains the total device footprint, limiting the scope of chip functionality. Devices designed to have a specific outcome can account for these constraints and overcome them with sufficient characterization and modeling. Microfluidic device designers can use finite element analysis (FEA) programs such as COMSOL Multiphysics, equipped with computational fluid dynamics (CFD) software packages, to computationally model the dynamic behavior of their device under convection, diffusion, and reactive conditions. This type of study is beneficial for quickly iterating through many different digital designs in order to identify a smaller set of designs that produce the best outcome in a computational model. The designer can then fabricate and test the best performing design to validate if the computational and empirical outcomes match. Employing digital manufacturing techniques in this fashion allows for a significant amount of device development to be done without the high labor costs associated with fabrication, testing, and troubleshooting. This workflow was used to iterate through many different diffusion-based gradient generator designs before fabricating a single design that addressed the needs of a cell-based investigational study.

The 3D, spatiotemporal gradient generating platform relies on SL's ability to produce complex 3D shapes to allow for selective diffusion of biomolecules to a gel-containing channel. The device consists of three channels: one gel channel that lies between two reagent channels. The reagent channels interface with the gel channel via 3D windows. Depending on the design, these windows vary in surface area to allow selective amounts of mass transport at different geometric locations on the gel. The critical innovation of the device is the fact that the gel channel has a very high length-to-width aspect ratio allowing rapid generation of diffusion-based gradients across the entire volume of the gel via its width, instead of length. In addition, the gel is able to fill the central channel without overflowing into the adjacent reagent channels through the use of phase guide pillars that pin the meniscus of the high surface tension gel back [44].

5.1 Methods

Computational models of the gradient generator platform were created in COMSOL Multiphysics as a time dependent, three-dimensional, transport of diluted species model, wherein carboxyfluorescein (376.32 g/mol) diffused through an aqueous solution ($\mathcal{D}$ = 4.9E-10 m^2/s, [45]) from a constant concentration source (100 μM) to a constant concentration sink (0 μM). The transport of diluted species model follows the partial differential relation of the diffusion equation:

$$\frac{\partial \phi(r,t)}{\partial t} = \nabla \cdot [\mathcal{D}(\phi, r)\nabla\phi(\mathrm{r,t})] \qquad \textit{Eq. 3}$$

where $\phi(r,t)$ is the density of the diffusing species at location r and time t, and $\mathcal{D}(\phi, r)$ is the collective diffusion coefficient for density ϕ at location r. However, by assuming that $\mathcal{D}$ is constant, the equation reduces to a linear differential equation:

$$\frac{\partial \phi(r,t)}{\partial t} = \mathcal{D}\nabla^2\phi(\mathrm{r,t}) \qquad \textit{Eq. 4}$$

which is identical to the heat equation. This model was applied to three different geometric components each representing the gel channel and reagent channel diffusion windows for different design configurations of the gradient generating microfluidic platform. A concentration evaluation midline was used to quantify the generated gradient's evolution over time. These computational models are shown in Figure 13.

An empirical test was run on one of these device configurations to corroborate the computational model's predicted gradient generation. The gradient generating device with the largest gel volume channel was fabricated with the Asiga Pico 2 HD in 0.6/0.6 PEGDA-258 using the 50 μm layer height settings shown in Table 1. The device schematic and experimental setup/results are shown in Figure 14. The device was tested by loading warm, 2 wt.% agarose in water into the gel channels via tubing that connected the device's connector and a gel-loaded syringe. Coupled with the slow delivery of the gel, the diffusion window pillars induced phase guiding, which created meniscus pinning that prevented side-channel overflow. Once the gel had filled approximately 75% of the channel length, the remainder was filled using the connector on the opposite side of the device. The

gel channel's open roof allows for gel to overflow after filling the channel. The gel retracts away from the substrate during gel curing/cooling, which in turn forms micropores in the diffusion windows upon which fluid in the reagent channel can escape via convection. To avoid this outcome, the gel was cured only after overflowing the device with excess gel on the roof; this excess gel acted to refill any micropores that may have formed during curing. The 2 wt.% agarose gel-loaded device was cured in a 3 °C refrigerator for 15 minutes. Before device operation, the excess cured gel was cut away with a razor, and the surface of the roof of the device was covered and bonded to PDMS via an acrylate-functionalizing linker (see Appendix 8.3). Then, the reagent channel connectors were used to slowly load blue dye into the two exterior reagent channels and yellow dye into the interior reagent channel. Lastly, after the channels were filled with dye and diffusion had begun, tubing with plugged connectors were added to prevent any fluid evaporation through the device's connectors.

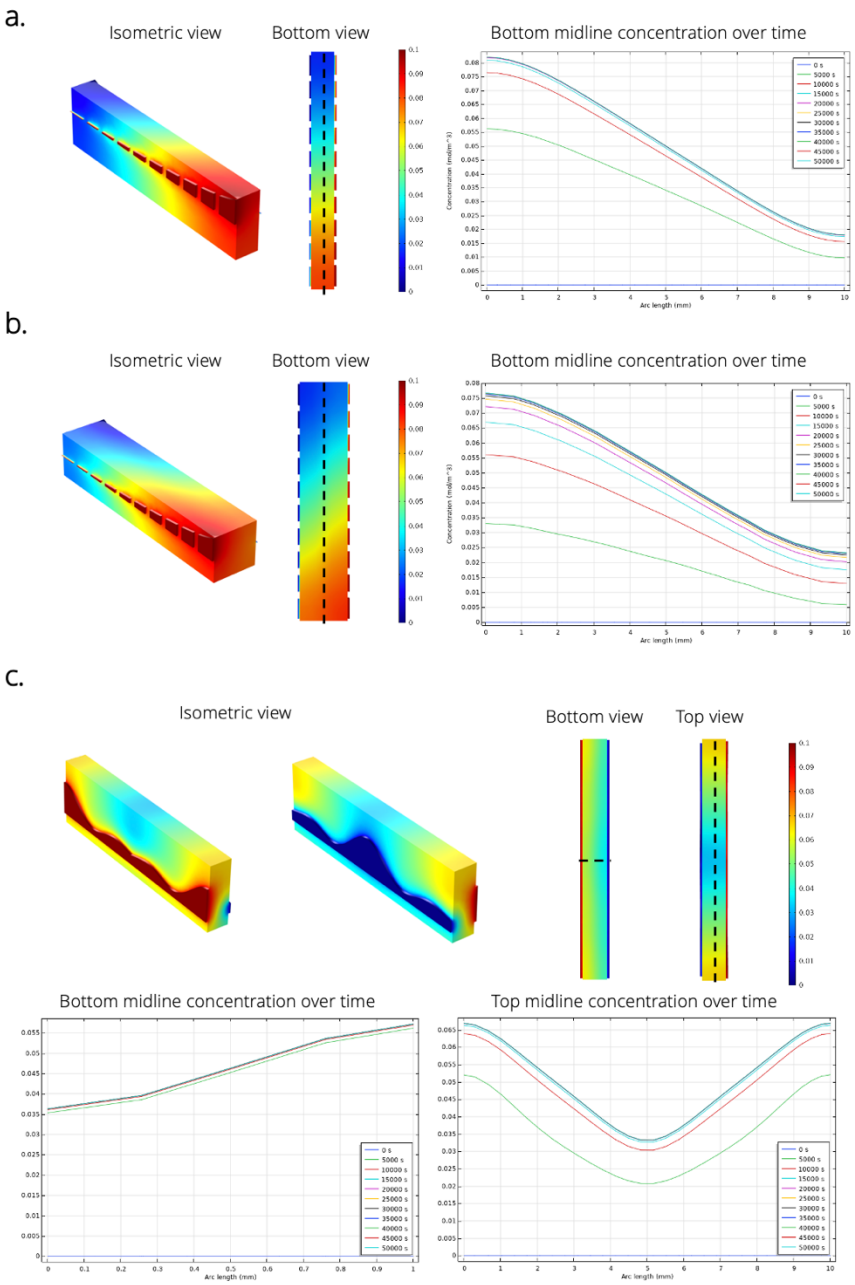

Figure 13: Finite element analysis models of fluorescein diffusion in gradient generating designs. (a.) Reverse exponential diffusion windows in a (1 mm x 10 mm x 2.5 mm) gel with windows spaced 300 µm apart to represent SL printed pillars. Isometric and bottom views of the gel-containing channel show the established gradient at steady state. The dashed line in the bottom view was the conc. evaluation midline used to assess the established gradient along the length of the gel. At steady state, the gel reached a max. conc. of ~80% of the 100 µM fluorescein and a min. conc. of ~20% at the other end of the device, achieving 90% of its steady state conc. by 2.77 hours. (b.) Reverse exponential diffusion windows in a (2 mm x 10 mm x 2.5 mm) gel with windows spaced 300 µm apart to represent SL printed pillars. At steady state, the gel reached a max. conc. of ~76% of the 100 µM fluorescein and a min. conc. of ~24% at the other end of the device, achieving 90% of its steady state conc. by 3.33 hours. (c.) Reverse sinc diffusion windows in a (1 mm x 10 mm x 3 mm) gel. Steady state along the width of the bottom of the gel reached a max. conc. of 56% of the 100 µM fluorescein on one side of the device and a min. conc. of ~36% on the other, achieving 90% of its steady state conc. within 1 hour. Steady state along the length of the top of the gel reached a max. conc. of 66% of the 100 µM fluorescein on one end of the device and a min. conc. of ~34% at the other end of the device, achieving 90% of its steady state conc. by 1.94 hours.

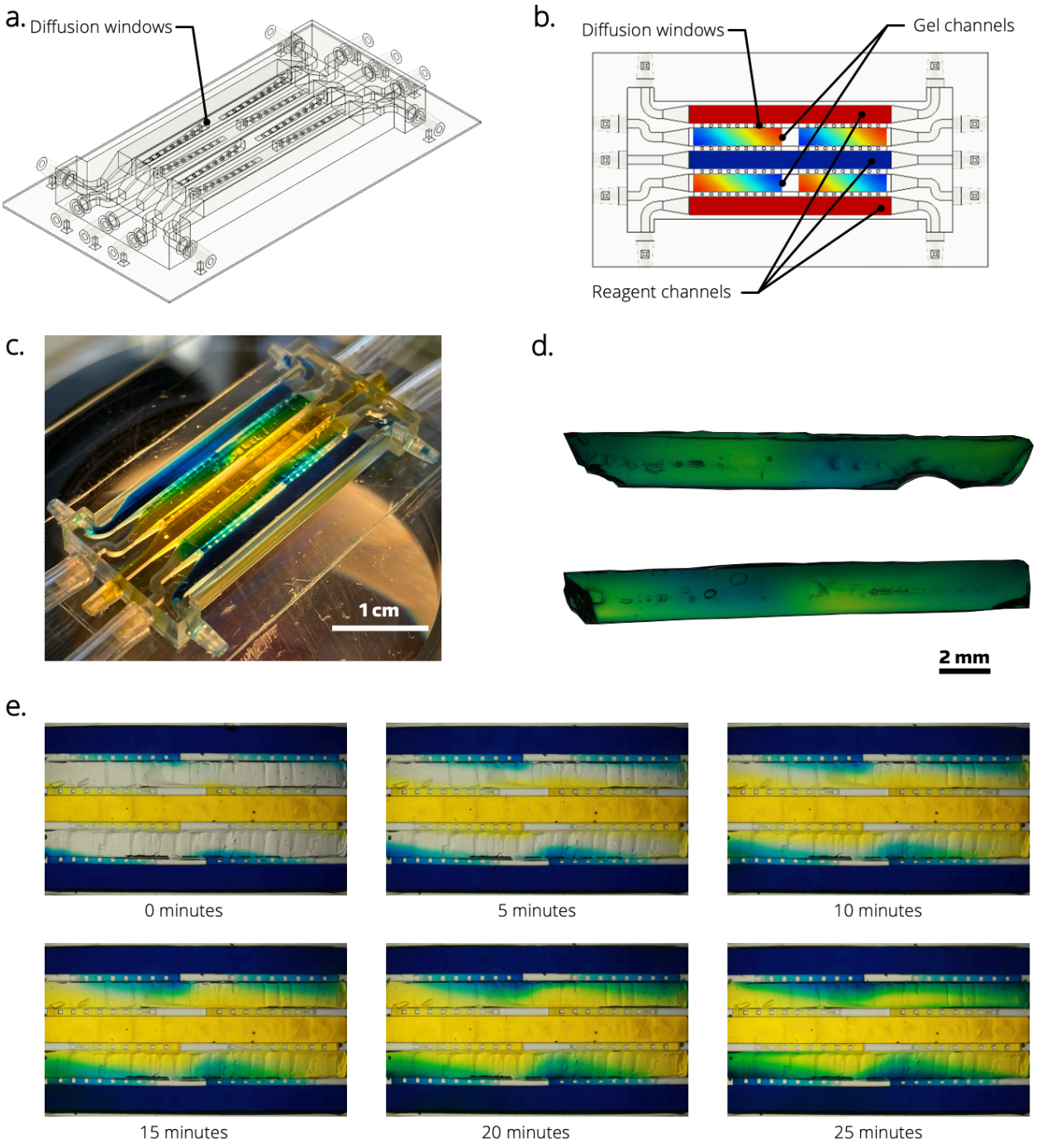

Figure 14: 3D spatiotemporal gradient generator platform schematic and experimental results. (a.) Isometric view of 5-channel, reverse exponential diffusion window microfluidic device. (b.) Top view of expected gradients across four (2 mm x 10 mm x 2 mm) gel regions: two in series and two in parallel. (c.) Image of the SL printed device loaded with blue dye on the exterior reagent channels, yellow dye on the interior reagent channel, and 2% agarose in the intermediate gel channels. Although the gel is atmosphere-exposed, a PDMS membrane is bonded to the top surface to minimize evaporation. (d.) The gel channel's open roof allows for gel removal after diffusion gradient window exposure. Selective patterning of blue and yellow dye can be observed from a side view in the gel sample extracted from this experiment. The profile of some of the diffusion windows can be seen as well. (e.) Diffusion gradient evolving over time within the microfluidic device.

5.2 Results and discussion

The FEA models made in COMSOL validated the hypothesis that selectively diffusing reagents along the width of a high length-to-width aspect ratio channel allows the rapid formation of complex, 3D spatiotemporal gradients. Multiple designs corroborated these findings, including those that included "pillars," or gaps between diffusion windows, to account for the manufacturing constraints of SL printed microfluidic devices. Several designs explored the generation of linear 3D gradients across a large volume of gel. When trying to produce such a gradient across a 1 mm x 10 mm x 2 mm gel, the diffusion equilibration time could take as much as 18 hours when diffusing along the length of the channel. With the approach demonstrated above, where diffusion is across the width of the gel, equilibration time is reduced to only ~3 hours. In addition, new, complex, 3D spatiotemporal gradients can be generated by utilizing unique geometrical shapes for the diffusion windows. The design shown in Figure 13c develops a linear gradient across the width of the gel's bottom surface and a parabolic gradient across the length of the gel's top surface. The interpolation of these two gradients forms complex concentration isosurfaces within the gel volume. Due to their novelty, these complex gradients do not yet have an established biological application. Thus, a series of exploratory studies should be conducted that broadly investigate the effect on different cell-in-gel systems. SL enables the widespread dissemination, experimentation, and prototyping of microfluidic devices, which is especially useful for developing a new technological paradigm for gradient generation.

One possible application of these devices is optimizing induced pluripotent stem cell (iPSC) growth factor concentrations through the generation of large-scale linear gradients on culturing cells. In collaboration with Dr. Vincenzino Cirulli from the Institute for Stem Cell & Regenerative Medicine (ISCRM), I developed a gradient generating platform that could house large volumes (> 100 μL) of cell-containing gel. Dr. Cirulli informed the Folch lab that his standard iPSC experimental protocol yields milliliters worth of cells that must undergo an experimental treatment. Although the reverse exponential diffusion window design shown in Figure 13b was larger than previous iterations, it still

only consisted of a 50 μL gradient-exposed gel region - too low for it to be worth generating iPSCs. To improve upon the volume capability of the gradient generator design, I designed a microfluidic device that multiplexed the delivery of one reagent channel to four gradient-exposed gel regions. The device is shown in Figure 14. Based on the diffusion window exposed region of 2 mm x 10 mm x 2 mm, the total gel volume exposed to gradient generation in this device is 160+ μL. This configuration proves to be more useful for iPSC experimentation because it can produce a higher yield of gradient-treated cells. Currently, Dr. Cirulli is integrating the SL printed device with his standard iPSC cultures to determine effects on cell viability and physiology. After, he will use the device as intended and impart growth factor gradients on culturing iPSCs to see if cells exhibit different behaviors because of the relative spatial concentration of growth factor they receive in culture.

While device design and fabrication are critical to repeated experimentation and development, so too is device operation. As I gained experience operating these gradient generators, I identified several challenges that must be solved to improve experiment success. The most pressing issue is that of evaporation on device functionality. As described in 5.1 Methods, gel retraction away from the 3D window leaves pores for fluid flow to occur directly into and around the gel channel. This outcome effectively ends the experiment as any fluid interface outside the designated diffusion window will fundamentally change the gradient being generated. These devices are meant to be operated with fluid in them for extended durations (e.g. 1 day for dye-based experiments or 14 days for iPSC experiments). However, open contact to air even on short time scales (< 1 hour) causes water to evaporate from the device, which causes gel retraction. This effect occurred during the dye test shown in Figure 14: the gel in the diffusion window on the bottom reagent channel gradually retracted as the experiment ran. By minute 30, the blue dye flowed completely around the entire gel channel via wicking. I attempted to mitigate this problem by bonding a PDMS membrane on the roof of the gel channels as well as plugging the connectors leading to the gel channels, but evaporation still managed to occur. Therefore, more extensive experimental controls must be implemented to

ensure the gel does not retract from the diffusion window; this may include running the device in a high humidity chamber or continuously flowing reagents along the reagent channels. The next challenge is that of reagent exchange, or ensuring that the concentration of the species of interest is "constant" at the interface to the diffusion window. The FEA models relied on the assumption that the concentration for one set of diffusion windows was constant at 100 μM fluorescein and the other set of diffusion windows was always at 0 μM fluorescein. Though this is a simple assumption to make for a computational model, this assumption does not hold empirically, especially over long time scales. New computational models should be made that analyze this effect by having a fixed volume and concentration of solute available for diffusion. Then, empirical experiments should be run that compare gradients generated from devices that have undergone solute exchange and those that have not. These initial tests are promising and show the potential that these devices have for generating complex 3D gradients. With further optimization and development, the Folch lab can use these devices to investigate a whole new range of complex biological processes that would not have been possible before for organ-on-a-chip to drug screening applications.

6. A microfluidic microneedle array for high throughput delivery of iPSCs

Recent advances in stem cell therapy have enabled the repair and improvement of heart muscle function by directly delivering iPSC-derived cardiomyocytes (iPSC-CMs) to infarcted heart tissue [46]. Most studies of cardiac cell transplantation have used direct intramyocardial injection under surgical visualization [47], [48]. Although these initial works have yielded positive results, they are limited by the manually directed single-needle approach used for iPSC-CM delivery into tissues. The operator cannot reliably control both depth and distribution of cell delivery while the host's myocardium is beating. As much as 80% of cells can be lost during the injection process. As such, there is a need to develop a new approach for iPSC delivery into the myocardium that dispenses cells at a specific depth, uniformly distributes them across the affected tissue, and minimizes the waste of injected cells. Microfluidic microneedle arrays have already been designed and printed for use in transdermal drug delivery [49], [50]. In collaboration with Allison Zech and Dr. Stephen Seslar from Seattle Children's Hospital, this work aims to extend the 3D printed microfluidic microneedle array technology to intramyocardial iPSC delivery.

The microfluidic microneedle array was designed to interface directly to a syringe equipped with a luer-lock/slip seal connector to ease handling and operation. The first iterations of the array were designed to have 64 microneedles, either 1 mm or 1.5 mm in length, spaced 1.25 mm apart. Each needle was individually addressable by a 200 μm wide by 400 μm tall microchannel that stemmed from a binary arbor channel network. The fluidic array's isometric and top view schematics are shown in Figure 15a and Figure 15b. Two different needle tips were tested for delivery and fabrication: beveled and conical. The bevel needle was designed to replicate the 29-gauge needle commonly used for iPSC-CM delivery. The conical needle was a new concept meant to deliver iPSC-CMs bilaterally through two 160 μm wide orifices, thereby creating a higher density iPSC-CM pattern with the same number of needles. The needle arrays were fabricated by Boston Micro Fabrication (BMF) using their microArch S140 printer and biocompatible resin: BIO. Zech conducted *ex vivo* tests

of the 1 and 1.5 mm long, beveled and conical needle arrays on the ventricular and atrial walls of a fresh, untreated porcine heart. These tests revealed that the needle arrays were very fragile, often breaking during the attempt at tissue puncture. In addition, the needle arrays failed to puncture the heart tissue, evenly deforming the tissue across all the needles instead.

Design and manufacturing changes were implemented to try and address these tissue puncture issues. One hypothesis for the lack of tissue penetration was that the density of the needle array evenly distributed the puncture force being driven by the user pushing the syringe into the heart tissue. Under this hypothesis, the puncture force per needle in the array would be less than that of the single-needle approach. This decreased force would result in the deformation of the heart tissue rather than its tearing or puncture. A newly designed microneedle array was produced to test this hypothesis: the needle density was reduced from 64 to 16, making the new needle spacing 2.5 mm apart, and the needle length was increased to 3 mm. The newly designed microneedle array was also fabricated by BMF using their microArch S140 printer, but the material used for this iteration was their highest stiffness resin: GR. The beveled and conical needle arrays are shown in Figure 15c. Zech performed the same *ex vivo* puncture test with these new designs, revealing that the lower density needle arrays could puncture the porcine heart. However, the thin hard plastic needles were not rigid enough to withstand the forces associated with puncture into the tough porcine heart tissue; many of the needles were sheared upon removal, breaking away from the needle array and embedding into the heart tissue. Zech explored an alternative microneedle fabrication approach that involved selective laser sintering of metal instead of SL.

The limitations surrounding material rigidity with SL printing are no longer relevant when fabricating microneedles out of metal. Zech modified the design of the microfluidic microneedle array to combine the best features of both materials. The schematic of these changes and images of the assembled final product is shown in Figure 16. The microneedle's design was adjusted to include 16 beveled needles on a flat plate, with female connectors underneath the needles to allow for a fluidic

channel interface between the metal needles and the plastic microfluidic base. The length of the microneedles had to be reduced to 2 mm because of the fabrication constraints of the selective laser sintering machine used by the fabricator, MetShape. The microfluidic base was designed to maintain the fluidic architecture that delivers fluid from the slip-seal connector to the needles. However, in the place of the needles are male connectors that facilitate a fluidic channel interface between the metal needles and the plastic microfluidic base. The microfluidic base was fabricated by BMF using their microArch S140 printer and GR resin. After using liquid adhesive to seal these two parts together, Zech attempted the *ex vivo* puncture test. The hybrid-material microfluidic microneedle array was able to puncture the porcine heart's ventricular wall successfully. Unfortunately, the main drawback with this device approach is that MetShape has yet to optimize its sintering process to produce a hollow needle reliably due to occlusion issues. One possible alternative Zech could investigate moving forward is using fine milling bits on CNC mills to create microfluidic through holes into solid metal microneedles fabricated via MetShape. Nonetheless, like SL printing, fabrication settings can be optimized to produce progressively better sintering outcomes. I am confident that the metal microneedle approach is worth further investigation and troubleshooting, given the advantages associated with the material's structural rigidity.

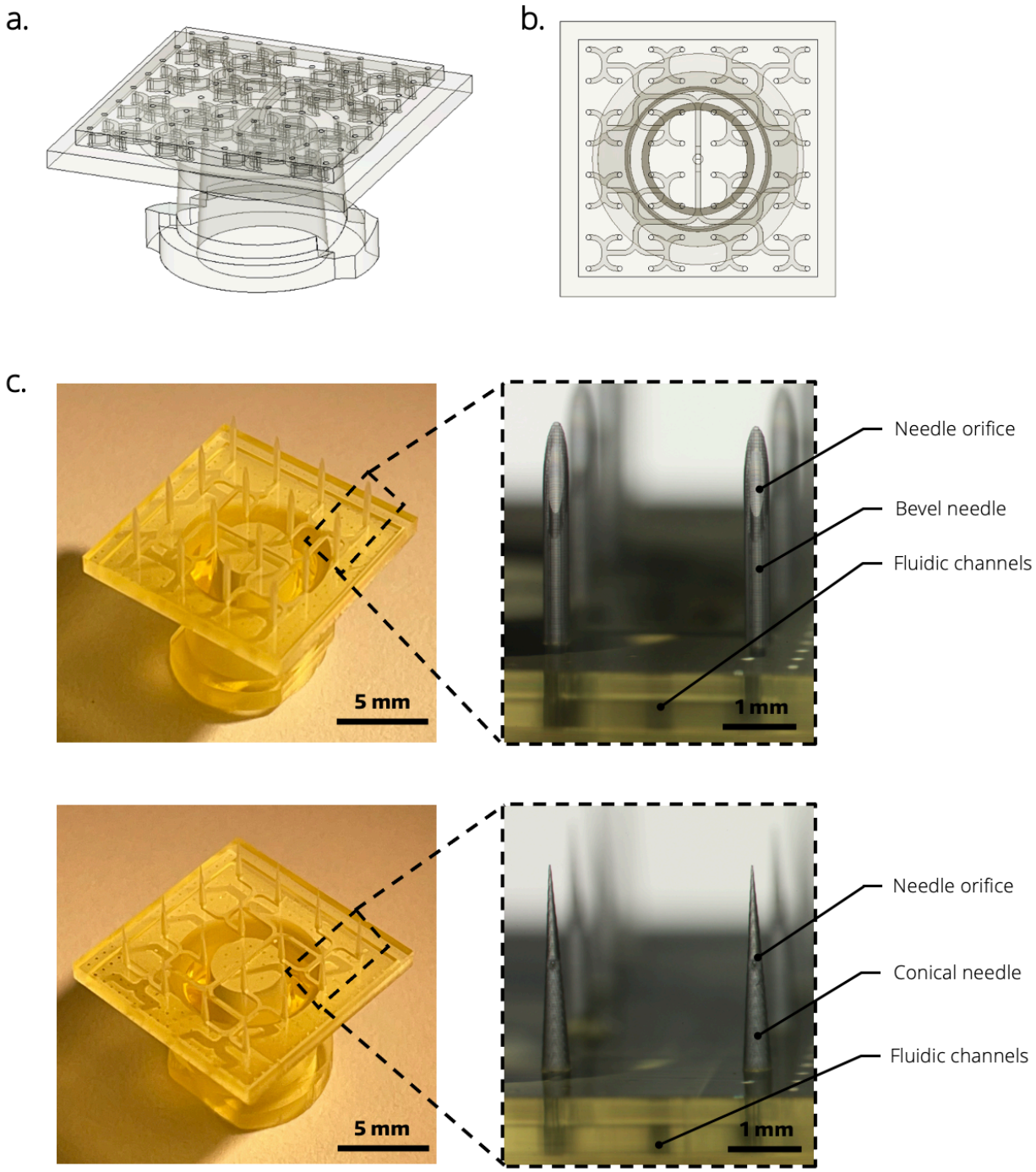

Figure 15: SL printed microfluidic microneedle array. (a.) Isometric view of fluidic architecture schematic for the 64-needle array. (b.) Top view of fluidic architecture schematic for the 64-needle array. (c.) Images of SL printed, 3 mm tall, 16-needle microfluidic microneedle arrays. (Top) Beveled needle design. (Bottom) Conical needle design.

a.

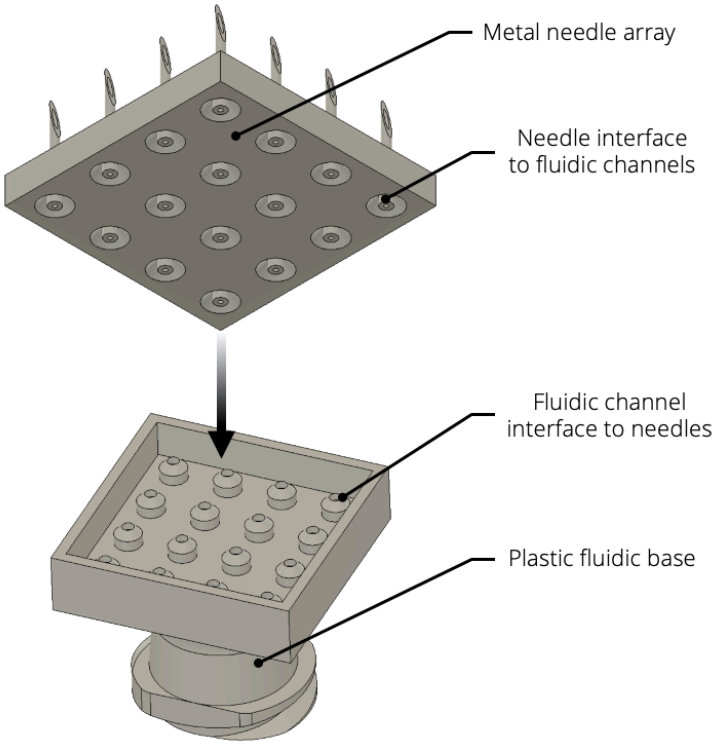

b.

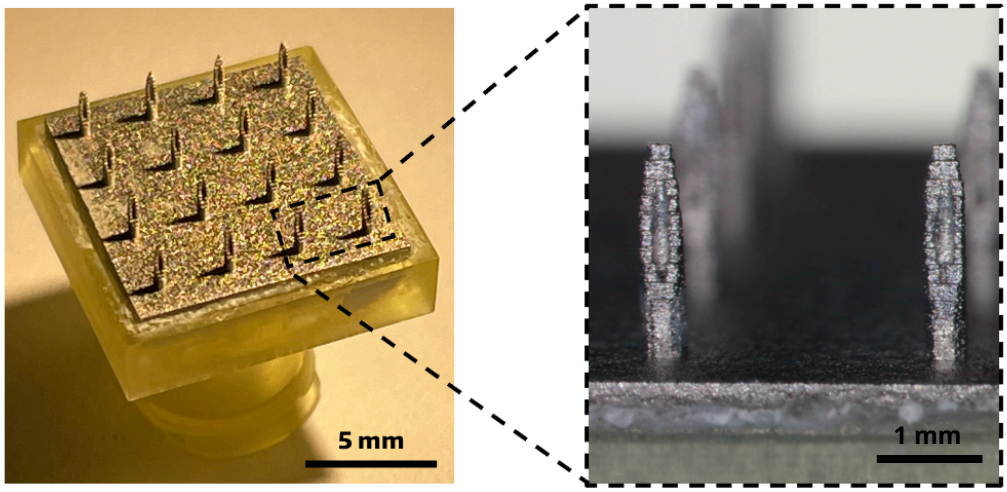

Figure 16: Selective laser sintered, metal microneedle array interfacing with an SL printed, hard plastic microfluidic base assembly. (a.) Metal microneedle array assembly procedure with the plastic microfluidic base. Alignment of the fluidic channel connectors on both the microneedle array and microfluidic base allow the formation of a continuous channel between the slip-seal luer lock connector on the plastic microfluidic base and the microneedles on the metal microneedle array. The two parts are sealed to one another via a small amount of liquid adhesive. (b.) Images of the selective laser sintered, 2 mm tall, 16-needle microneedle array interfacing with the SL printed, microfluidic plastic base.

7. Conclusion and future works

As organ-on-a-chip research becomes more mainstream, greater effort is being placed into creating *in vitro* systems that more accurately represent the complexity of *in vivo* biology. The *in vitro* tools that once propelled the growth of biological research in the 20th century are now simply insufficient for the intricate biological systems we aim to recreate today. Once considered a niche research specialty, microfluidics is now widely accepted as the essential tool for the next generation of life science research. Micromolded PDMS has carried microfluidics to where it is today because of its advantageous properties like high-resolution patterning, biocompatibility, and optical transparency. However, the disadvantages associated with its manufacturability, and thus its rapid prototypability, limit the prospect of using PDMS for microfluidics of the future. This work aimed to demonstrate the advantages of digital manufacturing and specifically SL for the production, testing, and development of microfluidic devices with the novel material and design complexity required for upcoming organ-on-a-chip research.

The most fundamental property of photopolymeric materials used for SL is that they are intrinsically modular, meaning that any individual molecular component can be exchanged with an alternative. Materials with vastly different properties can be created by simply exchanging or adding a monomer, photoinitiator, or photoabsorber. This feature has immense implications for biological studies as materials can be created and optimized for a specific application. I was able to display this principle by adding a biofunctional monomer to a hard plastic resin formulation. By showing the release of 2-mercaptopyridine after 150 mM GSH was introduced to 10 wt.% PDS-UM in 0.6/0.6 PEGDA-258, I demonstrated the covalent functionalization of GSH onto a 3D-printable hard plastic. Although this initial experiment does not have a practical biological application, it validated the idea that it is possible to have a modular functionalization platform built into the polymer network of a 3D printed microfluidic device. The upcoming experiments are clear: prove that a biotin-streptavidin based functionalization platform can be built onto the polymer network of PEGDA-258, and use that

bioorthogonal reactive chemistry to selectively functionalize the surface with cell adhesion molecules. Further work needs to be done to characterize why COMA did not perform as expected. However, the flexibility of SL platforms allows rapid prototyping of materials to achieve a desired outcome. Once a resin or hydrogel formulation is definitively determined to work with COMA, SL print settings can be optimized around that formulation. Simply by changing out resin formulations, SL enables the chemical modification of microfluidic structures in a way that is unmatched by PDMS micromolding processes.

The capabilities of a microfluidic device produced by SL not only depend on the material but also the design. As demonstrated in this work, SL can produce high-resolution structures in all three spatial dimensions, enabling the fabrication of unique structures that can only be fabricated through SL. The C2C12-in-gel culture device, although unsuccessful in its biological application, was still a novelty in terms of microfluidic device fabrication due to its low aspect ratio channels and ability to interface those channels directly to a syringe. Furthermore, the patterning of thin (81 μm) hard plastic fenestrations across a 10 mm by 10 mm area is unique to stereolithography. This device can be used to culture cells over long durations with further post-processing steps or minor resin composition changes. The gradient generating platform is another example of device design that is only possible through stereolithography. The formation of the 3D diffusion windows in patterns determined by a digital design can introduce limitlessly complex gradients across the gel channel. While the operation of these gradient generators still needs optimization, these devices show much promise for investigating never-before-seen biological phenomena. Lastly, the microfluidic microneedle area is yet another example of how microfluidics is becoming the tool of future biological treatments and technologies. The device itself is in its prototyping stages, but as fabrication technologies improve for SL and selective laser sintering, so too will the device's successful outcomes.

Through new materials testing and microfluidic device modeling, fabrication, and prototyping, I have demonstrated the promise of SL as an accessible and low-cost means for

improving the complexity of *in vitro* biological models. Although prior microfluidic technologies have been built around PDMS, the future of microfluidics depends on the capabilities of new manufacturing and prototyping technologies. The major limitations of SL, including resolution and resin biocompatibility, will inevitably be overcome as more groups try to create microfluidic devices that have increasing biological complexity. With sufficient integration into the bioengineer's toolbox, SL will spur a renaissance in the development of polymer chemistry, computational modeling, and cell biology.

8. Appendices

8.1 Acrylate silanization of glass slides procedure

1. Wash both surfaces of the glass slide with isopropanol.
2. Wash both surfaces of the glass slide with acetone.
3. Wash both surfaces of the glass slide with DI water.
4. Repeat for the remaining glass slides.
5. Use the air gun to blow off water on both surfaces of the glass slide.
6. Repeat for the remaining glass slides.
7. To remove any remaining water droplets, leave the glass slides in the oven for 30 min.
8. Oxygen plasma treat the glass slides for 2 min or corona treat both surfaces of the glass slide for 1 min.
9. Place an absorbent pad on a hot plate.
10. Pipette 0.5 mL of TMSPMA evenly across the absorbent pad.
11. Place the treated glass slides directly on top of the absorbent pad.
12. Cover the glass slides, absorbent pad, and hot plate in an enclosure.
13. Set the hot plate to 80 °C for 9 hours.

8.2 PEGDA-258 resin formulation procedure

0.6 wt.% OM819 and 0.6 wt.% ITX in PEGDA-258 was used as an example. Applies to other hard plastic formulations that use a powder photoinitiator and photoabsorber.

1. Wrap a falcon tube completely in aluminum foil.
2. Measure 0.33 g of OM819 photoinitiator (0.6 wt.% of 55 g).
3. Measure 0.33 g of ITX photoabsorber (0.6 wt.% of 55 g).
4. Measure up to 54.34 g of PEGDA-258 monomer (98.8 wt.% of 55 g).
5. Vortex the falcon tube and its contents.
6. Place the falcon tube in the oven at 80 °C for 20 min.

8.3 Acrylate silanization of PDMS procedure

1. Oxygen plasma treat the PDMS for 2 min or corona treat both sides of the PDMS for 1 min.
2. Prepare a TMSPMA treatment solution to have 98% ethanol-(70% in water), 1% TMSPMA, and 1% acetic acid.
3. Place treated PDMS in a petri-dish containing TMSPMA treatment solution.
4. Set the dish on a hot plate for 30 min to 3 hours at 80 °C.
5. Place air gunned-dry or wet PDMS on PEGDA device, ensuring there are no air bubbles.
6. Place PEGDA/PDMS into the UV box for 10 sec to 1 min.

8.4 PEGDA-700 hydrogel precursor formulation procedure

0.6 wt.% OM819, 0.6 wt.% ITX, and 30 wt.% PEGDA-700 in water was used as an example. Applies to other hydrogel formulations that use a powder photoinitiator and photoabsorber.

1. Wrap a falcon tube completely in aluminum foil.
2. Measure 0.33 g of OM819 photoinitiator (0.6 wt.% of 55 g).
3. Measure 0.33 g of ITX photoabsorber (0.6 wt.% of 55 g).
4. Measure 16.5 g of PEGDA-700 monomer (30 wt.% of 55 g).
5. Measure 37.84 g of DI water (68.8 wt.% of 55 g).
6. Vortex the falcon tube and its contents.
7. Place the falcon tube in the oven at 80 °C for 24 hours.

Note: OM819 and ITX are not soluble in water and will eventually crash out of solution after ~5 days. The hydrogel precursor is stable until that point because PEGDA-700 serves as an emulsifying agent. After the 24 hour oven incubation, the hydrogel precursor should appear as a cloudy emulsion. To avoid this problems, consider using polar photoinitiators and photoabsorbers instead.

9. References

[1] C. Jensen and Y. Teng, "Is It Time to Start Transitioning From 2D to 3D Cell Culture?," *Front. Mol. Biosci.*, vol. 7, 2020, doi: 10.3389/fmolb.2020.00033.

[2] F. Pampaloni, E. G. Reynaud, and E. H. K. Stelzer, "The third dimension bridges the gap between cell culture and live tissue," *Nat. Rev. Mol. Cell Biol.*, vol. 8, no. 10, Art. no. 10, Oct. 2007, doi: 10.1038/nrm2236.

[3] K. M. Mabry, S. Z. Payne, and K. S. Anseth, "Microarray analyses to quantify advantages of 2D and 3D hydrogel culture systems in maintaining the native valvular interstitial cell phenotype," *Biomaterials*, vol. 74, pp. 31–41, Jan. 2016, doi: 10.1016/j.biomaterials.2015.09.035.

[4] K. Kamei *et al.*, "Characterization of Phenotypic and Transcriptional Differences in Human Pluripotent Stem Cells under 2D and 3D Culture Conditions," *Adv. Healthc. Mater.*, vol. 5, no. 22, pp. 2951–2958, 2016, doi: https://doi.org/10.1002/adhm.201600893.

[5] D. Huh, Y. Torisawa, G. A. Hamilton, H. J. Kim, and D. E. Ingber, "Microengineered physiological biomimicry: Organs-on-Chips," *Lab. Chip*, vol. 12, no. 12, pp. 2156–2164, May 2012, doi: 10.1039/C2LC40089H.

[6] D. Huh *et al.*, "A Human Disease Model of Drug Toxicity–Induced Pulmonary Edema in a Lung-on-a-Chip Microdevice," *Sci. Transl. Med.*, vol. 4, no. 159, pp. 159ra147-159ra147, Nov. 2012, doi: 10.1126/scitranslmed.3004249.

[7] H. J. Kim, D. Huh, G. Hamilton, and D. E. Ingber, "Human gut-on-a-chip inhabited by microbial flora that experiences intestinal peristalsis-like motions and flow," *Lab. Chip*, vol. 12, no. 12, pp. 2165–2174, May 2012, doi: 10.1039/C2LC40074J.

[8] E. W. Esch, A. Bahinski, and D. Huh, "Organs-on-chips at the frontiers of drug discovery," *Nat. Rev. Drug Discov.*, vol. 14, no. 4, pp. 248–260, Apr. 2015, doi: 10.1038/nrd4539.

[9] S. Halldorsson, E. Lucumi, R. Gómez-Sjöberg, and R. M. T. Fleming, "Advantages and challenges of microfluidic cell culture in polydimethylsiloxane devices," *Biosens. Bioelectron.*, vol. 63, pp. 218–231, Jan. 2015, doi: 10.1016/j.bios.2014.07.029.

[10] K. J. Regehr *et al.*, "Biological implications of polydimethylsiloxane-based microfluidic cell culture," *Lab. Chip*, vol. 9, no. 15, pp. 2132–2139, Aug. 2009, doi: 10.1039/b903043c.

[11] Z. Zude, *Fundamentals of Digital Manufacturing Science*. Springer. Accessed: Jun. 04, 2021. [Online]. Available: https://www.springer.com/gp/book/9780857295637

[12] A. Waldbaur, H. Rapp, K. Länge, and B. E. Rapp, "Let there be chip—towards rapid prototyping of microfluidic devices: one-step manufacturing processes," *Anal. Methods*, vol. 3, no. 12, pp. 2681–2716, Dec. 2011, doi: 10.1039/C1AY05253E.

[13] A. Urrios *et al.*, "3D-printing of transparent bio-microfluidic devices in PEG-DA," *Lab. Chip*, vol. 16, no. 12, pp. 2287–2294, 2016, doi: 10.1039/C6LC00153J.

[14] A. K. Au, W. Lee, and A. Folch, "Mail-order microfluidics: evaluation of stereolithography for the production of microfluidic devices," *Lab. Chip*, vol. 14, no. 7, pp. 1294–1301, Apr. 2014, doi: 10.1039/c3lc51360b.

[15] N. Fang, C. Sun, and X. Zhang, "Diffusion-limited photopolymerization in scanning micro-stereolithography," *Appl. Phys. A*, vol. 79, no. 8, pp. 1839–1842, Dec. 2004, doi: 10.1007/s00339-004-2938-x.

[16] A. Bertsch, P. Bernhard, C. Vogt, and P. Renaud, "Rapid prototyping of small size objects," *Rapid Prototyp. J.*, vol. 6, no. 4, pp. 259–266, Jan. 2000, doi: 10.1108/13552540010373362.

[17] H.-W. Kang, I. H. Lee, and D.-W. Cho, "Development of an Assembly-free Process Based on Virtual Environment for Fabricating 3D Microfluidic Systems Using Microstereolithography Technology," *J. Manuf. Sci. Eng.*, vol. 126, no. 4, pp. 766–771, Feb. 2005, doi: 10.1115/1.1811116.

[18] C. I. Rogers, J. V. Pagaduan, G. P. Nordin, and A. T. Woolley, "Single-monomer formulation of polymerized polyethylene glycol diacrylate as a nonadsorptive material for microfluidics," *Anal. Chem.*, vol. 83, no. 16, pp. 6418–6425, Aug. 2011, doi: 10.1021/ac201539h.

[19] A. P. Kuo, N. Bhattacharjee, Y.-S. Lee, K. Castro, Y. T. Kim, and A. Folch, "High-Precision Stereolithography of Biomicrofluidic Devices," *Adv. Mater. Technol.*, vol. 4, no. 6, p. 1800395, 2019, doi: https://doi.org/10.1002/admt.201800395.
[20] H. Gong, M. Beauchamp, S. Perry, A. T. Woolley, and G. P. Nordin, "Optical approach to resin formulation for 3D printed microfluidics," *RSC Adv.*, vol. 5, no. 129, pp. 106621–106632, Dec. 2015, doi: 10.1039/C5RA23855B.
[21] M. Pagac *et al.*, "A Review of Vat Photopolymerization Technology: Materials, Applications, Challenges, and Future Trends of 3D Printing," *Polymers*, vol. 13, no. 4, Feb. 2021, doi: 10.3390/polym13040598.
[22] G. M. Cruise, D. S. Scharp, and J. A. Hubbell, "Characterization of permeability and network structure of interfacially photopolymerized poly(ethylene glycol) diacrylate hydrogels," *Biomaterials*, vol. 19, no. 14, pp. 1287–1294, Jul. 1998, doi: 10.1016/s0142-9612(98)00025-8.
[23] H. Lin, T. Kai, B. D. Freeman, S. Kalakkunnath, and D. S. Kalika, "The Effect of Cross-Linking on Gas Permeability in Cross-Linked Poly(Ethylene Glycol Diacrylate)," *Macromolecules*, vol. 38, no. 20, pp. 8381–8393, Oct. 2005, doi: 10.1021/ma0510136.
[24] J. A. Beamish, J. Zhu, K. Kottke-Marchant, and R. E. Marchant, "The effects of monoacrylated poly(ethylene glycol) on the properties of poly(ethylene glycol) diacrylate hydrogels used for tissue engineering," *J. Biomed. Mater. Res. A*, vol. 92, no. 2, pp. 441–450, Feb. 2010, doi: 10.1002/jbm.a.32353.
[25] Y.-S. Lee, N. Bhattacharjee, and A. Folch, "3D-printed Quake-style microvalves and micropumps," *Lab. Chip*, vol. 18, no. 8, pp. 1207–1214, Apr. 2018, doi: 10.1039/C8LC00001H.
[26] M. D. Volder and D. Reynaerts, "Pneumatic and hydraulic microactuators: a review," *J. Micromechanics Microengineering*, vol. 20, no. 4, p. 043001, Mar. 2010, doi: 10.1088/0960-1317/20/4/043001.
[27] A. K. Au, H. Lai, B. R. Utela, and A. Folch, "Microvalves and Micropumps for BioMEMS," *Micromachines*, vol. 2, no. 2, Art. no. 2, Jun. 2011, doi: 10.3390/mi2020179.
[28] H. Makamba, J. H. Kim, K. Lim, N. Park, and J. H. Hahn, "Surface modification of poly(dimethylsiloxane) microchannels," *Electrophoresis*, vol. 24, no. 21, pp. 3607–3619, Nov. 2003, doi: 10.1002/elps.200305627.
[29] D. V. V, B. S, and C. L, "Wettability increase by 'corona' ionization.," *Langmuir ACS J. Surf. Colloids*, vol. 27, no. 15, pp. 9614–9620, Jun. 2011, doi: 10.1021/la2019583.
[30] H. Chen, M. A. Brook, H. D. Sheardown, Y. Chen, and B. Klenkler, "Generic Bioaffinity Silicone Surfaces," *Bioconjug. Chem.*, vol. 17, no. 1, pp. 21–28, Jan. 2006, doi: 10.1021/bc050174b.
[31] J. L. Fritz and M. J. Owen, "Hydrophobic Recovery of Plasma-Treated Polydimethylsiloxane," *J. Adhes.*, vol. 54, no. 1–4, pp. 33–45, Nov. 1995, doi: 10.1080/00218469508014379.
[32] J. Dommerholt, F. P. J. T. Rutjes, and F. L. van Delft, "Strain-Promoted 1,3-Dipolar Cycloaddition of Cycloalkynes and Organic Azides," in *Cycloadditions in Bioorthogonal Chemistry*, M. Vrabel and T. Carell, Eds. Cham: Springer International Publishing, 2016, pp. 57–76. doi: 10.1007/978-3-319-29686-9_4.
[33] S. P. Black, J. K. M. Sanders, and A. R. Stefankiewicz, "Disulfide exchange: exposing supramolecular reactivity through dynamic covalent chemistry," *Chem. Soc. Rev.*, vol. 43, no. 6, pp. 1861–1872, Feb. 2014, doi: 10.1039/C3CS60326A.
[34] T. N. Gevrek *et al.*, "Facile Fabrication of a Modular 'Catch and Release' Hydrogel Interface: Harnessing Thiol–Disulfide Exchange for Reversible Protein Capture and Cell Attachment," *ACS Appl. Mater. Interfaces*, vol. 10, no. 17, pp. 14399–14409, May 2018, doi: 10.1021/acsami.8b00802.
[35] J. S. Miller, C. J. Shen, W. R. Legant, J. D. Baranski, B. L. Blakely, and C. S. Chen, "Bioactive hydrogels made from step-growth derived PEG–peptide macromers," *Biomaterials*, vol. 31, no. 13, pp. 3736–3743, May 2010, doi: 10.1016/j.biomaterials.2010.01.058.

[36] H. Vandenburgh *et al.*, "Tissue-engineered skeletal muscle organoids for reversible gene therapy," *Hum. Gene Ther.*, vol. 7, no. 17, pp. 2195–2200, Nov. 1996, doi: 10.1089/hum.1996.7.17-2195.
[37] C. Rhim *et al.*, "Morphology and ultrastructure of differentiating three-dimensional mammalian skeletal muscle in a collagen gel," *Muscle Nerve*, vol. 36, no. 1, pp. 71–80, 2007, doi: 10.1002/mus.20788.
[38] C. Snyman, K. P. Goetsch, K. H. Myburgh, and C. U. Niesler, "Simple silicone chamber system for in vitro three-dimensional skeletal muscle tissue formation," *Front. Physiol.*, vol. 4, p. 349, 2013, doi: 10.3389/fphys.2013.00349.
[39] H.-W. Kang, S. J. Lee, I. K. Ko, C. Kengla, J. J. Yoo, and A. Atala, "A 3D bioprinting system to produce human-scale tissue constructs with structural integrity," *Nat. Biotechnol.*, vol. 34, no. 3, pp. 312–319, Mar. 2016, doi: 10.1038/nbt.3413.
[40] B. Lin and A. Levchenko, "Spatial Manipulation with Microfluidics," *Front. Bioeng. Biotechnol.*, vol. 3, 2015, doi: 10.3389/fbioe.2015.00039.
[41] S. K. W. Dertinger, D. T. Chiu, N. L. Jeon, and G. M. Whitesides, "Generation of Gradients Having Complex Shapes Using Microfluidic Networks," *Anal. Chem.*, vol. 73, no. 6, pp. 1240–1246, Mar. 2001, doi: 10.1021/ac001132d.
[42] P. Herzmark *et al.*, "Bound attractant at the leading vs. the trailing edge determines chemotactic prowess," *Proc. Natl. Acad. Sci.*, vol. 104, no. 33, pp. 13349–13354, Aug. 2007.
[43] C. Joanne Wang, X. Li, B. Lin, S. Shim, G.-L. Ming, and A. Levchenko, "A microfluidics-based turning assay reveals complex growth cone responses to integrated gradients of substrate-bound ECM molecules and diffusible guidance cues," *Lab. Chip*, vol. 8, no. 2, pp. 227–237, Feb. 2008, doi: 10.1039/b713945d.
[44] P. Vulto, S. Podszun, P. Meyer, C. Hermann, A. Manz, and G. A. Urban, "Phaseguides: a paradigm shift in microfluidic priming and emptying," *Lab. Chip*, vol. 11, no. 9, pp. 1596–1602, May 2011, doi: 10.1039/C0LC00643B.
[45] E. M. Kramer, N. L. Frazer, and T. I. Baskin, "Measurement of diffusion within the cell wall in living roots of Arabidopsis thaliana," *J. Exp. Bot.*, vol. 58, no. 11, pp. 3005–3015, 2007, doi: 10.1093/jxb/erm155.
[46] Y.-W. Liu *et al.*, "Human embryonic stem cell-derived cardiomyocytes restore function in infarcted hearts of non-human primates," *Nat. Biotechnol.*, vol. 36, no. 7, pp. 597–605, Aug. 2018, doi: 10.1038/nbt.4162.
[47] J. J. H. Chong *et al.*, "Human Embryonic Stem Cell-Derived Cardiomyocytes Regenerate Non-Human Primate Hearts," *Nature*, vol. 510, no. 7504, pp. 273–277, Jun. 2014, doi: 10.1038/nature13233.
[48] H. Hamdi *et al.*, "Cell delivery: intramyocardial injections or epicardial deposition? A head-to-head comparison," *Ann. Thorac. Surg.*, vol. 87, no. 4, pp. 1196–1203, Apr. 2009, doi: 10.1016/j.athoracsur.2008.12.074.
[49] A. Doraiswamy *et al.*, "Two photon induced polymerization of organic-inorganic hybrid biomaterials for microstructured medical devices," *Acta Biomater.*, vol. 2, no. 3, pp. 267–275, May 2006, doi: 10.1016/j.actbio.2006.01.004.
[50] S. D. Gittard, A. Ovsianikov, B. N. Chichkov, A. Doraiswamy, and R. J. Narayan, "Two-photon polymerization of microneedles for transdermal drug delivery," *Expert Opin. Drug Deliv.*, vol. 7, no. 4, pp. 513–533, Apr. 2010, doi: 10.1517/17425241003628171.